# NUMERICAL AND EXPERIMENTAL INVESTIGATION OF A VERTICAL $LiBr$ FALLING FILM ABSORBER CONSIDERING WAVE REGIMES AND IN PRESENCE OF MIST FLOW

E. García-Rivera[a], J. Castro[a], J. Farnós[a], A. Oliva[a]

[a] *Centre Tecnològic de Transferéncia de Calor (CTTC), Universitat Politécnica de Catalunya (UPC), ETSEIAT, Colom 11, E08222 Terrassa (Barcelona), Spain*

**Abstract**

The absorber represents the most critical component in absorption systems and one of the key issues. In this component complex heat and mass transfer phenomena during the absorption process takes place simultaneously. For this reason the development of mathematical models validated against experimental data always constitutes useful tools for the design and improvement of falling film absorbers. A testing device has been designed and built to reproduce absorption phenomena in vertical $LiBr - H_2O$ falling film absorbers with the primary objective to obtain experimental data. On the other hand, a mathematical model of falling film absorption of $H_2O$ vapour in $LiBr$ aqueous solutions has been implemented. Wave regime is considered by including and solving the Free Surface Deflection Equation. The numerical results are validated using the experimental data.

During the development of this work, the authors have paid careful attention to the verification of experimental data. Such verification consists of performing energy and mass balances in the fluid film side. Important discrepancies were found in our experimental data. Therefore, an extensive study was carried out in order to find the source of such errors. The conclusion is that there is a drag of $LiBr$ solution in the water vapour which increases with the $Re$ number. This mist flow cannot be measured experimentally, but can be evaluated in an indirect way. The mathematical models have been adapted in order to consider the influence of mist flow. On the other hand, in the literature there are not many experimental works related to falling film absorbers which expose enough information to verify the reli-

ability of their experimental data.

*Keywords:*
absorption, LiBr, vertical falling film, wavy regime, numerical, experimental

---

## 1. Introduction

Absorption refrigeration technology has become more attractive in recent years. This is due to both the increasing price of primary energy, and the necessity of a more efficient decentralized energetic model. However, absorption technology has not been extended enough. The main impediment is the high initial investment required. In order to develop low-cost absorption machines of small capacity, the initial investment must be reduced. This is possible if the cooling tower is removed from the system. Therefore, air-cooled absorbers and condensers is a topic of technological interest. This is the reason why we give especial emphasis on studying the absorber under air-cooled conditions.

The absorber is usually the largest element of absorption machines due to its low heat and mass transfer coefficients. This fact determines the design of the whole system. Vertical falling film absorbers are an optimal solution of air-cooled systems [1–4]. In such devices the heat and mass transfer processes are produced simultaneously.

One of the earliest modelling attempts was published by Grigoreva and Nakoyarkov [5]. The authors consider the case of steady absorption in a smooth laminar falling film in an isothermal, impermeable vertical plate. A constant profile is assumed in streamwise velocity. Heat and mass transport are described by solving energy and species equations in two spatial dimension under the following assumptions: i) mass and thermal diffusion are negligible in the stream-wise direction; ii) the transverse velocity is negligible. Using these simplifying assumptions the authors provide a solution by means of Fourier separation variables techniques. Grossman [6] uses essentially the same simplifying assumptions as Grigoreva and Nakoyarkov [5]. However, he uses a parabolic velocity profile and a different boundary condition at the inlet (inlet solution temperature is equal to the wall temperature). Thus, no thermal boundary layer develops from the wall). Grossman uses two methods to solve the problem. First, using the Fourier method as in [5], he seeks a series expansion solution. Secondly, he uses a numerical technique based on finite difference method.

On the same line, Brauner et al. [7] presents a solution valid near the inlet region using similar technique as in reference [5]. Brauner's contribution is the application of Fick's law of diffusion at the interface without assuming infinite dilution in the liquid film. Andberg [8] is probably one of the first attempts to develop a solution for the horizontal tube case. The hydrodynamic of the falling film is divided into different regions, which are solved individually in the streamwise direction. Boundary layer approximations of the Navier Stokes equations are applied using finite difference techniques. Finally, Kawae et al. [9] develop a finite difference model to laminar similar to [8], but applied to vertical falling-film. The main differences are: i) thermophysical properties are not constant; ii) fully developed parabolic stream-wise velocity profile; iii) transverse velocity equal to zero.

In this work, a systematic research approach based on numerical modelling and experimental validation has been followed. On the one hand, an experimental setup which reproduces vertical falling film absorption, has been designed and built, $LiBr - H_2O$ is used as working fluid. The absorption process is controlled adjusting the following independent variables: solution concentration, solution temperature, cooling water temperature, absorber pressure and solution mass flow. The versatility of the experimental setup allows to manipulate independent variables for producing many experimental data of heat and mass transfer ratios under a wide variety of flows/conditions. The mass and heat absorbed are calculated by performing a mass and energy balances, respectively. An untypical situation has been detected during the experimental data reduction. It has been proved that water vapour drags some $LiBr$ micro drops from the generator to the absorber. This situation generates a kind of mist flow which increases as Re increases. The quantity of mist flow can only be evaluated in an indirect way. It is quantified using the "volumetric fraction" concept. Section 2.3 explains in detail the study in which this conclusion is reached, and the different actions that were taken in order to avoid this undesired situation. In the literature, no author mentions this untypical situation. However, some authors show important inconsistencies in their experimental data ([4, 10–12]).

On the other hand, a mathematical model of falling film absorption of $H_2O$ by $LiBr$ aqueous solutions has been implemented. The model is semi-empirical, based on Navier-Stokes equations together with energy and mass species simplified under the boundary layer hypotheses. The coupled equations are solved by means of the finite difference method in a step by step procedure. Another issue to be taken into consideration is the wavy regime in

a vertical falling film. Experimental observation shows that wavy regime appears even in low Reynolds number ($Re \approx 20$) [13, 14]. It is also well known that wavy regime causes increase of diffusion and mass transfer [15–18]. For this reason, wavy profiles are implemented together with falling film formulation. In the mathematical model, the Free Surface Deflection Equation is solved in each grid step for every Reynolds number, which is recalculated in function of mass absorbed. The mathematical model has been modified in order to consider the mist flow (see section 2.3).

## 2. Experimental Set-Up Description

The experimental setup and its main components are shown in Fig.1. The container (V1) is situated at the top of the structure. It has a capacity of approximately 17 litres (V1). It works as a generator, and it uses both an immersion heater of 2 kW and a set of Flexible Silicone Rubber Heaters placed directly on the outer surface with a total heating capacity of 4.4 kW. Each one of the heat generation sources is governed by an independent PID control. Therefore, each of them can be operated independently or simultaneously. The difference between using the immersion heater or flexible rubber heaters consists of the heat flux density ($\frac{W}{m^2}$ ) which provides each of the heaters. The absorber (A) is a single vertical tube, with a 0.022 m outer diameter and 0.018 m inner diameter. In order to visualize the absorption process, the vertical absorber is situated inside a borosilicate glass cover with a 0.315 m diameter and 1.5 m length. Two metal plates coupled with flat O-rings of nitrile-butadiene rubber (NBR) are situated both at the top and bottom of the glass container. The vertical absorber tube passes through the upper metal plates. Therefore in order to assure the sealing between the tube and the plate, an O-ring (NBR) is placed coupled with a flange. The measuring instruments used are as follows: Resistance Temperature Detectors (RTD), Coriolis mass flow-meters and densimeters (C1, C2, C3) and pressure sensors (PS1, PS2). Other components are: gear pumps (P1, P2, P3, P7), peristaltic pump (P6), vacuum pumps (P4,P5), thermal baths (TB1, TB2), plate heat exchanger (HX). There are three different circuits in the experimental apparatus: (i) $LiBr$ aqueous solution, (ii) $H_2O$ vapour and (iii) $H_2O$ coolant. The circuit (i) begins in (V1) where the $LiBr$ aqueous solution is heated, and water vapour is generated. The temperature in (V1) is controlled by (RTD1). The rich solution is pumped from the generator and it passes across a heat exchanger (HX), where points 1 and 2 represent

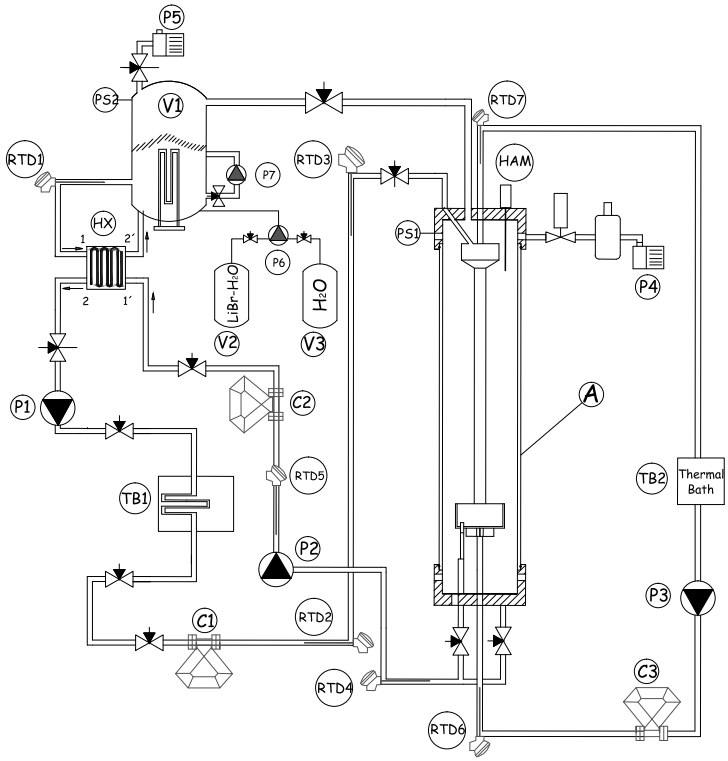


Figure 1: Falling Film Experimental Apparatus.

the inlet and the outlet of the plate heat exchanger.

The inlet mass flow and density are measured by (C1), the rich solution enters at the top of the absorber where it is collected in the dispenser which creates the falling film on the outer side of the vertical tube. While the fluid is flowing down, the absorption phenomenon is produced. The bottom dispenser picks up the weak solution which is sent back to the generator using the gear pump (P2). Both mass flow and density of the outlet solution are measured by (C2). The solution passes across (HX), where points $1'$ and $2'$ represent the inlet and the outlet of the plate heat exchanger respectively. The water vapour flows from the top of the generator to the absorber. During the generation process, the pump (P7) recirculates the aqueous solution. This is useful in order to maintain a homogeneous temperature inside the generator. Both absorption and generation pressures are

measured using the pressure gauges (PS1) and (PS2), respectively. Since concentration is an important factor, it is necessary to adjust it in a accurate way. A peristaltic pump (P6), together with vessels (V2) and (V3), are used to establish concentration. (V3) contains $H_2O$, while (V2) contains highly concentratred $H_2O - LiBr$ solution. Using the pump (P6) it is possible to increase or decrease the concentration in the generator by adding either $H_2O$ or $H_2O - LiBr$ solution. Both concentration of the rich and the poor solution can be calculated since $c = f(\rho, T)$. Thus, (RTD2) and (RTD5) are used for obtaining concentrations while (RTD3) and (RTD4) are used for calculating an energy balance in the absorber. The coolant circuit is fed directly by the thermal bath (TB2), where the inlet temperature can be adjusted, and the coolant fluid is pumped in counter-flow. On the other hand, an energy balance in the coolant fluid is performed using (RTD6) and (RTD7). The thermal bath (TB1) is used to adjust the inlet temperature of the rich solution. During absorption process, this is a key issue to maintain this temperature under control due to its influence in the absorption process. Finally, the vacuum pumps (P4) and (P5), together with a liquid nitrogen cold trap, are used for removing non-absorbable gases. In order to avoid problems of condensations with RTD measurements for the vapour temperature, the authors have used an thermistor coupled with the optical sensor (HAM) in order to obtain more accurate measurements.

### *2.1. Data Reduction*

In order to ensure the reliability of the experimental data, energy and mass balances are performed in the $LiBr - H_2O$ vertical falling film absorber (see Fig.2):

$$\dot{m}_{l,in} h_{l,in} + \dot{Q}_{abs,v} = (\dot{m}_{l,in} + \dot{m}_{abs,v}) h_{l,out} + \dot{Q}_{abs,c} \tag{1}$$

$$\dot{m}_{l,in} c_{in} = (\dot{m}_{l,in} + \dot{m}_{abs,v}) c_{out} \tag{2}$$

$$\dot{m}_{c,in} h_{c,in} + \dot{Q}_{abs,c} \;\; = \;\; \dot{m}_{c,out} h_{c,out} \tag{3}$$

The equation (1) represents the energy balance in the whole absorber (falling film side). The term ($\dot{Q}_{abs,c}$) represents the total heat load that is

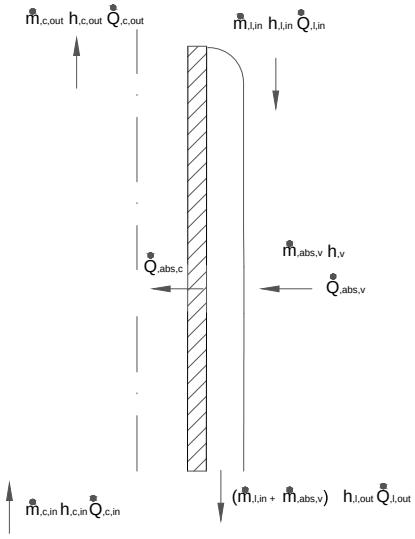


Figure 2: Schematic representation of the mass and energy balances in falling film and coolant fluids.

removed from the coolant side. ($\dot{Q}_{abs,v}$) is energy input through the interface coming from the water vapour, and $\dot{m}_{abs,v}$ is the mass of vapour water absorbed by the $LiBr - H_2O$ liquid film. The equation (2) represents the mass balance in the falling film side. This is used for calculating the mass absorbed ($\dot{m}_{abs,v}$). The equation (3) represents an energy balance on the coolant side. It is used for calculating the heat load ($\dot{Q}_{abs,c}$). The only unknown in equation (1) is the term ($\dot{Q}_{abs,v}$). Moreover, the energy input through the interface $\dot{Q}_{abs,v}$ can also be calculated using the following exp ression:

$$\dot{Q}_{abs,v} \approx \dot{m}_{abs,v} h_v(T_v, P_{abs}) \tag{4}$$

The reliability of the experimental data involves the calculation of the energy input through the interface $\dot{Q}_{abs,v}$ using equation (1) and equation (4). When comparing both quantities, the difference should not exceed the uncertainty analysis error.
In section 2.3 some discrepancies between the equations (1) and (4) are shown. This fact has been confirmed in the experimentation by the detection of microdroplets formed by $LiBr - H_2O$. Therefore the equation (1) needs to be rewritten as follows:

$$\dot{m}_{l,in}h_{l,in} + \dot{Q}_{abs,v} + \dot{Q}_{abs,l} = (\dot{m}_{l,in} + \dot{m}_{abs,v} + \dot{m}_{abs,l})h_{l,out} + \dot{Q}_{abs,c} \quad (5)$$

where,

$$\begin{aligned} \dot{Q}_{abs,v} &= \dot{m}_{abs,v}h_v(T_v, P_{abs}) & (6)\\ \dot{Q}_{abs,l} &= \dot{m}_{abs,l}h_l(T_{gen}, c_{in}) & (7)\\ \dot{Q}_{abs,c} &= \dot{m}_c(h_{c,out} - h_{c,in}) & (8) \end{aligned}$$

The term $\dot{m}_{abs,v}$ refers to the mass absorbed by water vapour, while the term $\dot{Q}_{abs,v}$ refers to the energy flow associated with such mass flux. Analogously, the term $\dot{m}_{abs,l}$ is the total mass of aqueous solution of mist flow which enters in the absorber. The term $\dot{Q}_{abs,l}$ is the heat input associated with the mist flow. Finally, the term $\dot{Q}_{abs,c}$ refers to the total heat load removed by the coolant side.

The mass balance in the film side yields:

$$\begin{aligned} \dot{m}_{l,in} + \dot{m}_{abs,v} + \dot{m}_{abs,l} &= \dot{m}_{l,out} & (9)\\ \dot{m}_{l,in}c_{in} + \dot{m}_{abs,l}c_{in} &= \dot{m}_{l,out}c_{out} & (10) \end{aligned}$$

In equation (9) the total mass fluxes in the film side are reflected. Equation (10) represents the $LiBr - H_2O$ mass fluxes. Solving equations (5) - (10) it is possible to calculate both mass fluxes, $\dot{m}_{abs_v}$ and $\dot{m}_{abs_l}$. In order to evaluate the amount of total mist flow which enters in the absorber, the concept of volumetric void fraction is introduced.

$$X = \frac{\frac{\dot{m}_{abs,v}}{\rho_v}}{\frac{\dot{m}_{abs,v}}{\rho_v} + \frac{\dot{m}_{abs,l}}{\rho_l}} \quad (11)$$

Due to the fact that the liquid density is too large compared to vapour density ($\frac{\rho_v}{\rho l} \approx e^{-6}$), the value $X$ is expected to be too small ($\ll 1\%$). For this reason the unit of part per million (PPM) where $1 \cdot 10^4\ PPM = 1\%$ is used for plotting.

*2.2. Uncertainty analysis*

An uncertainty analysis was performed in order to evalute the confidence of our experimental data. The uncertainty analysis is based in the methodology suggested by Moffat [19]. For the calculation of the uncertainty in the mass absorbed, the following relation is used:

$$\Delta \dot{m}_{abs} = \sqrt{\left(\frac{\partial \dot{m}_{abs}}{\partial \dot{m}_{l,in}} \Delta \dot{m}_{l,in}\right)^2 + \left(\frac{\partial \dot{m}_{abs}}{\partial c_{in}} \Delta c_{in}\right)^2 + \left(\frac{\partial \dot{m}_{abs}}{\partial c_{out}} \Delta c_{out}\right)^2} \quad (12)$$

The error associated to the inlet solution mass flow $\dot{m}_{l,in}$ is directly obtained from precision of the Coriolis flowmeter. On the other hand, in order to calculate the error associated to the LiBr concentration, we have to express the dependence of this magnitude with respect to errors associated in the true experimental measured variables, density and temperature:

$$\Delta c = \sqrt{\left(\frac{\partial c}{\partial \rho} \Delta \rho\right)^2 + \left(\frac{\partial c}{\partial T} \Delta T\right)^2} \quad (13)$$

The following table gives numerical values for the uncertainty analysis in a set of experiments. The values of the partial derivatives of the function $c = f(\rho, T)$ Chua et al. [20] as to the density and concentration are given for the calculation:

| $Re$ | Experimental Data | | | Experimental Errors | | | Partial Derivatives | | | Results | |
|---|---|---|---|---|---|---|---|---|---|---|---|
| | $\dot{m}_{l,in}$ $(\frac{kg}{s})$ | $c_{in}$ | $c_{out}$ | $\dot{m}_{l,in_{Err}}$ $(\frac{kg}{s})$ | $c_{in,Err}$ | $c_{out,Err}$ | $\frac{\partial \dot{m}_{abs}}{\partial \dot{m}_{l,in}}$ $(\frac{kg}{s})$ | $\frac{\partial \dot{m}_{abs}}{\partial c_{in}}$ $(\frac{kg}{s})$ | $\frac{\partial \dot{m}_{abs}}{\partial c_{out}}$ $(\frac{kg}{s})$ | $\Delta \dot{m}_{abs}$ $(\frac{kg}{s})$ | $\dot{m}_{abs}$ $(\frac{kg}{s})$ |
| 89 | 6.894E-3 | 6.041E-1 | 5.889E-1 | 1.034E-5 | 2.455E-4 | 2.531E-4 | 2.581E-2 | 1.171E-2 | -1.201E-2 | 4.192E-06 | 1.7794E-4 |
| 100 | 7.666E-3 | 6.041E-1 | 5.898E-1 | 1.149E-5 | 2.456E-4 | 2.515E-4 | 2.424E-2 | 1.300E-2 | -1.331E-2 | 4.634E-06 | 1.8587E-4 |
| 129 | 9.850E-3 | 6.039E-1 | 5.930E-1 | 1.478E-5 | 2.458E-4 | 2.502E-4 | 1.838E-2 | 1.661E-2 | -1.691E-2 | 5.887E-06 | 1.8105E-4 |
| 158 | 1.199E-2 | 6.034E-1 | 5.952E-1 | 1.798E-5 | 2.459E-4 | 2.494E-4 | 1.378E-2 | 2.014E-2 | -2.042E-2 | 7.108E-06 | 1.8518E-4 |
| 194 | 1.468E-2 | 6.030E-1 | 5.969E-1 | 2.202E-5 | 2.459E-4 | 2.486E-4 | 1.022E-2 | 2.459E-2 | -2.484E-2 | 8.647E-06 | 1.5002E-4 |
| 225 | 1.696E-2 | 6.026E-1 | 5.984E-1 | 2.544E-5 | 2.461E-4 | 2.481E-4 | 0.702E-2 | 2.834E-2 | -2.854E-2 | 9.941E-06 | 1.1903E-4 |

Table 1: Experimental data at different $Re$ numbers considering the presence of mist flow.



| $Re$ | Experimental Data | | | | Partial Derivatives | | | Results |
|---|---|---|---|---|---|---|---|---|
| | $\dot{m}_{c,in}$ $(\frac{kg}{s})$ | $T_{c,in}$ $(\circ C)$ | $T_{c,out}$ $(\circ C)$ | $\dot{Q}_{abss,c}$ $(W)$ | $\frac{\partial \dot{Q}_{abs,c}}{\partial \dot{m}_{c,in}}$ $(\frac{J}{Kg})$ | $\frac{\partial \dot{Q}_{abs,c}}{\partial T_{c,in}}$ $(\frac{W}{\circ C})$ | $\frac{\partial \dot{Q}_{abs,c}}{\partial T_{c,out}}$ $(\frac{W}{\circ C})$ | $\Delta \dot{Q}_{abs,c}$ $(W)$ |
| 89 | 0.11 | 32.88 | 34.3 | 730.1 | 6161.1 | 493.31 | 493.31 | 55.822 |
| 100 | 0.11 | 32.88 | 34.3 | 731.1 | 6164.4 | 493.98 | 493.98 | 55.898 |
| 129 | 0.11 | 32.88 | 34.4 | 731.5 | 6178.2 | 494.25 | 494.25 | 55.929 |
| 158 | 0.11 | 32.88 | 34.3 | 721.3 | 6086.9 | 490.68 | 490.68 | 55.524 |
| 194 | 0.11 | 32.88 | 34.3 | 702.9 | 5926.6 | 491.53 | 491.53 | 55.621 |
| 225 | 0.11 | 32.88 | 34.3 | 661.5 | 5582.2 | 490 | 490 | 55.446 |

Table 2: Experimental data at different $Re$ numbers considering the presence of mist flow.

Appendix C shows a comparison of the mass absorbed calculations according to the different functions $c = f(\rho, T)$ from several authors. No important differences have been detected.

An analogous analysis has been performed for the uncertainty associated to the total heat load measured at the coolant side $\dot{Q}_{abs,c}$, see Table (2). For the calculation of the uncertainty associated, the following relation is used:

$$\Delta\dot{Q}_{abs,c} = \sqrt{\left(\frac{\partial\dot{Q}_{abs,c}}{\partial\dot{m}_{c,in}}\Delta\dot{m}_{c,in}\right)^2 + \left(\frac{\partial\dot{Q}_{abs,c}}{\partial T_{c,in}}\Delta T_{c,in}\right)^2 + \left(\frac{\partial\dot{Q}_{abs,c}}{\partial T_{c,out}}\Delta T_{c,out}\right)^2} \tag{14}$$

The average uncertainty in the heat load absorber measured on the coolant side ($\dot{Q}_{abs,c}$) was $\pm 6.36\%$. The average uncertainty in the mass absorbed $\dot{m}_{abs}$ for all the reported experimental data was $\pm 10.5\%$.

### *2.3. Experimental Study of Mist Flow*

This subsection is devoted to describing the experiments in which the presence of mist flow is confirmed. Two different tests have been performed. Table 3 shows the difference of the evaluation of the energy input through the interface ($\dot{Q}_{abs_v}$) between the equations (1) and (4). It is shown that the difference between both quantities increases when $Re$ increases. This tendency is repeated in each experimental test. It should be noted that the quantities calculated by the equation (1) are higher than values calculated by the equation (4), the maximum discrepancy is about 32%.

| Re | $\dot{Q}_{abs_v}$(W) Eq.(1) | $\dot{Q}_{abs_v}$ (W) Eq.(4) | Discrepancy(%) |
|---|---|---|---|
| 2.201e+02 | 5.039e+02 | 3.453e+02 | 31.48 |
| 1.899e+02 | 5.164e+02 | 4.207e+02 | 18.53 |
| 1.564e+02 | 5.141e+02 | 4.443e+02 | 13.58 |
| 1.294e+02 | 5.054e+02 | 4.709e+02 | 6.98 |
| 1.000e+02 | 4.925e+02 | 4.825e+02 | 2.03 |
| 8.990e+01 | 4.645e+02 | 4.620e+02 | 0.54 |

Table 3: Comparison of experimental energy input through the interface ($\dot{Q}_{abs_v}$). Equations (1) and (4).

In order to discard any measurement errors or sensor faults, a study was carried out on the sensors involved in data reduction. Individual and coupled tests of each circuit (primary and secondary) without generation of vapour were performed. The results obtained matched with the corresponding energy balance.

Listed below are the actions taken in order to discard measurement errors or sensor faults:

i An energy balance was performed in the coolant fluid side, (the primary fluid was not present) since there was no heat load ($T_{c_{in}} \approx T_{c_{out}}$), the results of the mass flow-meter ($C3$) were compared with anoother with the same precision.

ii An energy balance was performed in the aqueous solution side (the coolant side was not present). Since there was neither vapour generation nor heat removed from coolant fluid, the inlet solution temperature was approximately equal to the outlet solution temperature ($T_{s_{in}} \approx T_{s_{out}}$) and the inlet solution density is approximately equal to the outlet solution density ($\rho_{in} \approx \rho_{out}$).

iii An energy balance was performed in both the aqueous solution and coolant side (without generation of vapour). It was established that The inlet solution temperature was greater than the outlet coolant temperature ($T_{l_{in}} > T_{c_{out}}$). After applying the equations (2) and (1), the results of the mass absorbed and energy input through the interface $\dot{Q}_{abs,v}$ were lower than the measurement errors.

Furthermore, it can be concluded that the energy imbalance arrives when vapour water is generated. Two possible phenomena could explain this imbalance: i) heat transfer by convection from the water vapour towards the falling film interface; ii) aqueous solution dragged by the generation of water vapour. It creates vapour water containing suspended micro-drops (mist flow) of aqueous solution of $LiBr$.

The point (i) was discarted as the water vapour density is too low $\frac{\rho_v}{\rho l} \approx 1e^{-6}$, consequently the convective heat transfer coefficient is too low since $Nu = \frac{\alpha_v x}{\lambda_v} \sim Re \cdot Pr$ and $Re = \frac{\rho_v U x}{\mu_v}$, $Pr = \frac{\mu_v cp_v}{\lambda_v}$. Therefore the heat transfer can be considered negligible.

In order to confirm the presence of the mist flow into the water vapour flow, the authors have performed the following experimental test (see Fig.

4). Since the mist flow is formed in the generation process, a small vessel with water was installed in the vapour line, between the generator and the absorber. The vapour water enters at the bottom of the vessel, the mist flow mixes with the water, and drops with an almost pure concentration of water flow out at the top of the vessel.

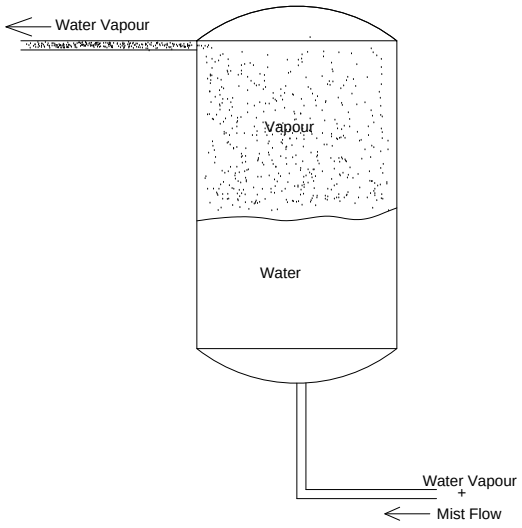


Figure 3: Schematic description of the vessel for mist flow.

Table 4 shows the results of the experimental test. The discrepancy between the equations (1) and (4) is still present. However, there is a significant difference in comparison with Table 3. When using the water vessel, the energy input through the interface ($\dot{Q}_{abs,v}$) calculated by the equation the equation (4) is higher than that one calculated using equation (1) (see the change of sign).

This is due to the mist flow still present, but it is formed by almost pure water. This can be explained from the point of view of the mass absorbed. We have two ways of measuring the mass absorbed: i) an overall mass balance (equation 1) which is a function of inlet and outlet concentrations. Such concentrations are obtained by means of the Coriolis densimeters; ii) an overall energy balance in the experiment (equations 1-4). We found discrepancies between both methods when mist flow of $LiBr$ solution is present. We have an extra contribution of mass flow liquid solution, and the measurement of the mass absorbed by means of the Coriolis of densimeters underestimates

the deduction of the mass absorbed (due to extra input of $LiBr$) obtained by means of the overall energy balance. When we have mist flow of pure water, the deduction of mass absorbed by means of the Coriolis overestimates the deduction of the mass absorbed (the total mass of $H_2O$ is equal to the vapour water absorbed, plus the total of the mist flow) which the mass absorbed obtained by the overall energy balance. There is mass "absorbed" of water which has not performed change of phase at the interface.

| Re Number | $\dot{Q}_{abs,v}$(W) Eq.(1) | $\dot{Q}_{abs,v}$ (W) Eq.(4) | Discrepancy(%) |
|---|---|---|---|
| 2.256e+02 | 3.920e+02 | 5.916e+02 | -33.74 |
| 2.006e+02 | 4.201e+02 | 5.601e+02 | -24.99 |
| 1.764e+02 | 4.401e+02 | 5.301e+02 | -16.97 |
| 1.464e+02 | 4.601e+02 | 5.201e+02 | -11.53 |
| 1.164e+02 | 4.801e+02 | 5.101e+02 | -5.88 |
| 8.164e+01 | 4.711e+02 | 4.810e+02 | -2.04 |

Table 4: Comparison of experimental energy input through the interface ($\dot{Q}_{abs,v}$) (water vessel). Equations (1) and (4).

A second experimental test has been performed. It consists of a rudimentary demister placed in the vapour line between the generator and the absorber. A small sponge of polyurethane is placed at the entrance of the vessel. The purpose is to trap the microdroplets suspended in the vapour flow. After performing the test, we found that the demister was displaced from its original position, this was due to the high velocities of the vapour. Furthermore, small amounts of the aqueous solution (about $20ml$) were found. This test confirms the presence of mist flow suspended in the vapour flow.

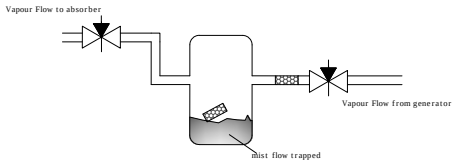


Figure 4: Schematic description of the experimetal trap-vessel for mist flow.

In the literature, there are some experimental works that reproduce falling film absorbers (vertical or horizontal). However, most of them do not divulge

enough data in order to check the consistency of their experimental measurements (see equations 1 - 4) [4, 10–12, 21–30]. Miller, in his Doctoral Dissertations [23], presents experimental data for vertical absorbers in smooth tubes. He shows discrepancies of approximately 30% of the total heat load between a range of Reynolds $200 - 310$. Miller et al. [10] present a technical report for vertical absorbers using advanced surfaces. They reported a range of $Re$ numbers between 26 to 80, the discrepancies between their energy balances are 5.85% ($Re \approx 26$) and 43.46% ($Re \approx 80$). In its experimental set-up, the water vapour water which enters into the absorber came directly from the generator. A fact to emphasize is that both works, the heat load calculated using the equation (1) is higher than the quantity related to the equation (4), as in the present work. On the other hand, Medrano et al. [4, 24] and Takamatsu et al. [12] do not consider in their experimental data reduction the $c_{out}$ measure. It is then calculated by solving the equations (1)-(4) in order to find the new value of $c_{out}$, which satisfies such equations. In this way, this fact makes it impossible to detect any unbalance in energy or mass in their experiment.

After an exhaustive review of the test device configuration, the possible explanations for the mist flow could be: i) large differences between generation and absorption pressures; ii) excessive nucleation during the generation procedure; iii) high vapour velocities provoked by high heat fluxes.

The authors have taken actions in order to avoid the above points: i) in order to prevent high heat fluxes, the solution was recirculated inside the generator and the generation area was increased; ii) the vapour circuit has been redesigned to decrease the vapour velocity.

Despite the taken actions, mist flow is still present. The reason was the way the vapour was generated, by means of an electrical resistance in the generator vessel that caused a heat flow too high and a nucleate boiling process. However, it is possible to calculate both the void fraction and the total mass flow of solution that enters into the absorber using the set of equations (5) - (10).

A comparison of the experimental results between equations (1) and (4) was performed in order to determine the maximum $Re$ where the mist flow has no influence. Fig. 5 shows the effects of Reynolds number ($Re \approx 90-270$) in $\dot{Q}_{abs,v}$ for equation (1) (black dots), and equation (4) (red dots) at different inlet mass concentrations ($c_{in} \approx 0.57 - 0.61\%$). The experimental results are depicted using the error bar calculated by the uncertainty analysis. An acceptable matching is considered when $Re < 150$.

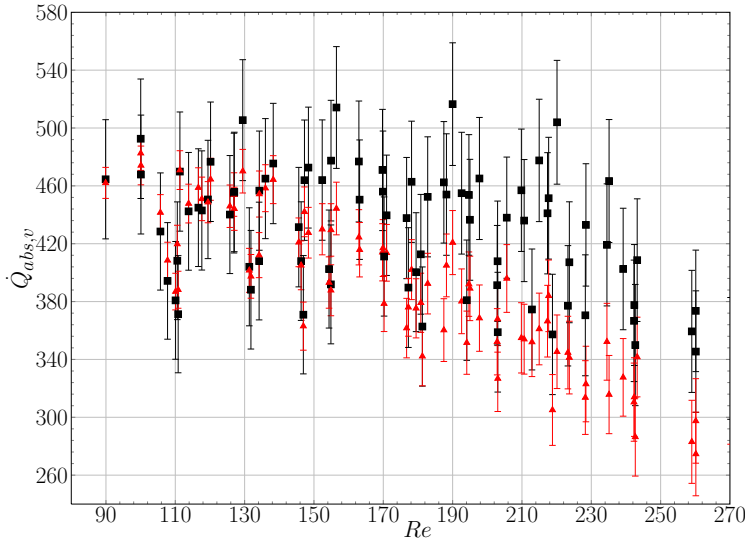


Figure 5: Effects of Reynolds number in $\dot{Q}_{abs,v}$ for equation the (1) (black dots), and the equation (4) (red dots) at different inlet mass concentrations.

Fig.6 is analogous to the previous Figure. It shows $\dot{m}_{abs,v}$ for equation (2) (black dots), and equation (4) (red dots) at different inlet mass concentrations ($c_{in} \approx 0.57 - 0.61\%$).

Finally Fig. 7 shows the discrepancy in (%) between equations (1) and (4). Discrepancies below 10 (%) are present when $Re < 150$. We consider these cases as free of mist flow.

## 3. Mathematical Formulation and Numerical implementation

The absorber is modelled as a single vertical tube. The falling film flow occurs when aqueous solution flows down in the outer part of the tube. The cooling water in counter flow is used in the inner part of the tube. The vertical tube is immersed in a water vapour environment, which is also introduced in the top part of the absorber. Fig.2 shows a scheme of the vertical absorber.

### *3.1. Boundary Layer model*

A similar model was originally proposed by Andberg [8]. However, it was implemented for the simulation of absorption in horizontal tubes. This

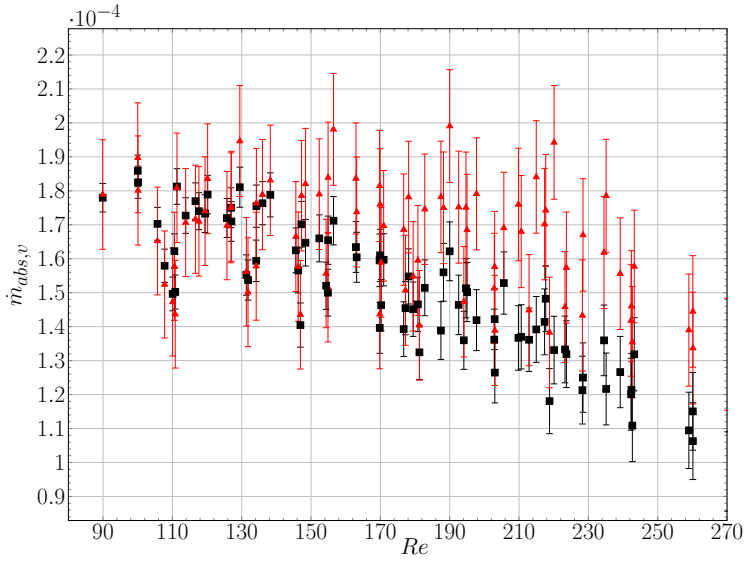


Figure 6: Effects of Reynolds number in $\dot{m}_{abs,v}$ for equation (1) (black dots), and equation (4) (red dots) at different inlet mass concentrations.

author distinguishes three different hydrodynamic regions, i) turning jet region, ii) turned jet region, iii) fully viscous film. The present work uses the same mathematical formulation as Andberg, but without taking into account region (i), and assuming totally fully viscous region due to the fact that vertical tubes are simulated. Fig. 8 shows details of the vertical falling film and its boundary conditions. A detailed treatment of the liquid-vapour interface boundary condition has been considered in order to take into consideration the influence of the mist flow phenomena described in section 2.3.

The following hypotheses are assumed in the calculation:

i Steady state flow.

ii The initial velocity considered corresponds to fully developed flow.

iii Physical properties variable only in the flow direction.

iv There is no shear stress at the interface.

v The radius of the tube is much greater than the falling film thickness. Therefore, curvature effects of the tube are neglected.

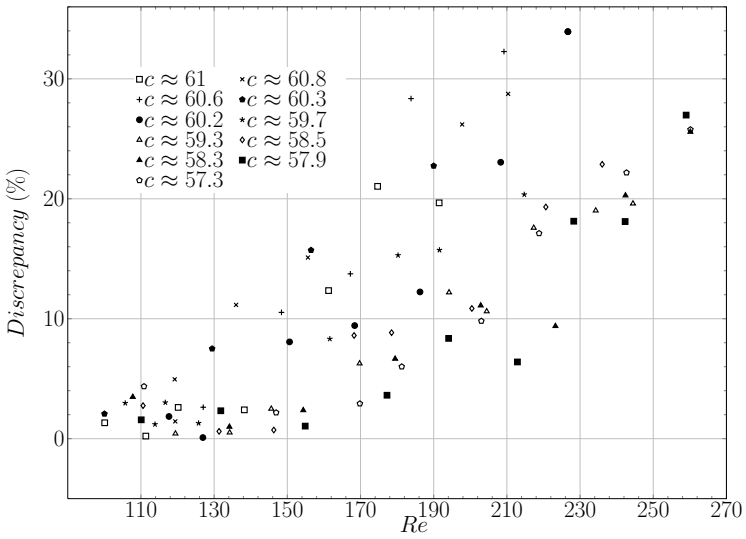


Figure 7: Effects of $Re$ in discrepancy rate (%) at different inlet solution mass concentrations.

vi There is thermodynamic equilibrium at the interface.

vii The flow can be both laminar smooth or wavy laminar and it is also incompressible.

viii The diffusion terms are negligible in the flow direction.

ix The convection terms are negligible in the direction orthogonal to the flow.

x The pressure gradients are negligible.

xi Dufour and Soret effects have not been considered.

xii Curvature effects in pressure due to wavy flow are neglected (capillary waves).

According to the above mentioned hypotheses, the governing conservation equations of mass (15), momentum (16), energy (17) and mass species (18) can be written as:

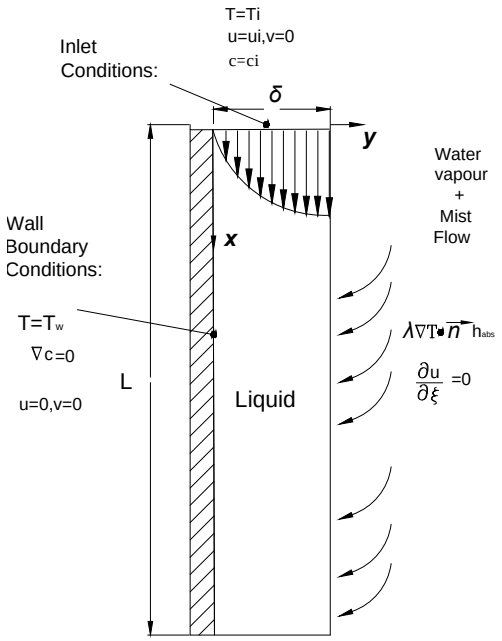


Figure 8: Boundary Conditions in Vertical Falling Film

$$\frac{\partial u}{\partial x} + \frac{\partial v}{\partial y} = 0 \tag{15}$$

$$u\frac{\partial u}{\partial x} + v\frac{\partial v}{\partial y} = gcos(\theta) + \nu\frac{\partial^2 u}{\partial y^2} \tag{16}$$

$$u\frac{\partial T}{\partial x} + v\frac{\partial T}{\partial y} = a\frac{\partial^2 T}{\partial y^2} \tag{17}$$

$$u\frac{\partial c}{\partial x} + v\frac{\partial c}{\partial y} = D\frac{\partial^2 c}{\partial y^2} \tag{18}$$

The partial differential equations system is solved by means of a change of coordinates taking into account the variation of the thickness of the falling

film. Due to the parabolic structure of the system of equations, the flow is solved in a step-by-step procedure. This model has already been tested for predicting absorption phenomena of $H_2O - LiBr$ systems with acceptable results[31, 32]. The boundary conditions are:

$$x = 0 \begin{cases} T_l = T_{l,in} & (a) \\ c = c_{in} & (b) \\ u = u_{l,in} & (c) \\ v = 0 & (d) \end{cases} \tag{19}$$

$$y = 0 \begin{cases} T = T_w & (a) \\ \nabla c \cdot \vec{n} = 0 & (b) \\ u = 0 & (c) \\ v = 0 & (d) \end{cases} \tag{20}$$

$$y = \delta \begin{cases} T_{l,if} = f(P_{abs}, c_{if}) & (a) \\ -\lambda \nabla T \cdot \vec{n} = h_{abs} \dot{m}_{abs,v} + h_l \dot{m}_{abs,l} & (b) \\ \frac{\partial u}{\partial \xi} = 0 & (c) \end{cases} \tag{21}$$

Equations (19 a-d) represent the inlet conditions, inlet solution temperature ($T_{l,in}$) and inlet mass concentration ($c_{l,in}$) are known data, and the inlet velocity solution ($u_{l,in}$) calculated by means of the solution of Nusselt's typical velocity profile. Equations (20 a-d) represent the wall boundary conditions, where $T_w$ is the wall temperature, and $\nabla c \cdot \vec{n} = 0$ depicts impermeable wall condition. Equations (21 a-c) describe the conditions of the interface, equation (21 a) describes thermodynamic equilibrium, equation (21 b) represents an energy balance in the liquid falling film interface. The convection heat transfer in the vapour side is neglected. Equation (21 c) indicates no shear stress at the interface. The mass absorbed from the vapour water, and the total mass of mist flow of aqueous solution can be calculated by means of the following expressions:

$$\dot{m}_{abs_{H_2O,t}} = \dot{m}_{abs,v} + \dot{m}_{abs_{H_2O,l}} \quad (22)$$

$$\dot{m}_{abs_{H_2O,l}} = \dot{m}_{abs,l}(1 - c_{in}) \quad (23)$$

$$\dot{m}_{abs_{H_2O,t}} = \frac{(1 - c_{if})\dot{m}_{abs_l} c_{in}}{c_{if}} + \frac{D\rho}{c_{if}} \nabla(1 - c) \cdot \vec{n} \quad (24)$$

Equation (22) describes the total mass flow of $H_2O$ which enters through the interface, equation (23) refers to a portion of water liquid of the mist flow, and finally equation (24) described by means of the Fick's law for a moving flow of the total mass flow of $H_2O$. In Appendix A there are further details about how the equation is obtained. The above equations together with equation (11) are solved in order to determine the four unknowns $(\dot{m}_{abs_{H_2O,t}}, \dot{m}_{abs_v}, \dot{m}_{abs_{H_2O,l}}, \dot{m}_{abs_l})$. The above set of expressions are a partial differential system of equations, and due to its parabolic nature, they can be solved using a step-by-step procedure. The following section provides details about the algorithm of resolution.

### *3.2. Wavy Regime Model*

One of the characteristics of the hydrodynamics in a vertical falling film is the wave phenomena in the free-surface flow. It is well known that wavy motion in falling liquid films significantly enhances the heat and mass transfer. Therefore, both experimentally and analytically by many authors [13–18, 33–45] have been investigated. The problem is not an easy issue from a numerical point of view, due to heat and mass transfer coupled problems and the presence and the unsteady behaviour of the wave motion. From a hydrodynamic point of view, the wave motion is a function of Reynolds number of the different flow regimes. Table 5 shows a brief description of falling film flow.

This work focuses on the capillary wavy laminar regime ($20 < Re < 200$). In literature, some of the most relevant studies of wavy phenomena in free surface are those that assume a periodic wave state. This assumption simplifies the mathematical derivation, and also provides enough confidence in numerical results. Yang [13] and Hirshburg [34] obtain the Free Surface Deflection Equation, assuming a parabolic profile of the streamwise velocity. The cross-stream velocity is then calculated from the conservation of mass.

| Flow Description | Reynolds Number |
|---|---|
| smooth film | $\mathrm{Re} \leq 20$ |
| capillary wavy laminar | $20 < \mathrm{Re} < 200$ |
| inertial wavy laminar (Roll waves) | $200 < \mathrm{Re} < 1000$ |
| inertial wavy turbulent | $1000 < \mathrm{Re} < 4000$ |
| fully turbulent | $\mathrm{Re} \geq 4000$ |

Table 5: Falling film flow description at different Reynolds numbers [14, 34, 39].

The velocity distributions are substituted into momentum equation and integrated across the film. In Fig. 9 the characteristic dimensions of the problem are shown. The wavelength of the wavy surface is $\Lambda$, the mean film thickness of the film over the wavelength is $\delta_o$, the characteristic velocity is defined as $U_o = \frac{\Gamma}{\rho_l \delta_0}$ and the wave number is $\psi = \frac{\delta_o}{\Lambda}$. Since the film thickness is too small compared to flow length, $\Lambda \gg \delta_o$ or $\psi \ll 1$, this simplifies the formulation.

Hirshburg [34] tried to extend the Free Surface Deflection Equation to higher Reynolds numbers where $\Lambda \sim \psi$. However, his mathematical formulation involves an uncertainty, and it becomes unpractical. Patnaik [14], Patnaik and Pérez-Blanco [38, 39] also present a mathematical model for roll waves in falling films for range value of $200 < Re < 1000$. The authors distinguish four different wave zones. Each zone is characterized by a film thickness function, which is obtained by Brackbill et al. [33]. A parabolic profile for the streamwise velocity is then assumed. This profile is function of the $x$ and $y$ coordinates, $t$, and the corresponding film thickness function. Thus, a different parabolic profile is obtained for each wave zone. The transverse velocity component is obtained by deriving the continuity equation. A periodic smooth function which passes through the known points is obtained with a three-term Fourier series.

As mentioned previously, this paper is based on the assumption of a periodic wave state, [13, 34–36, 43, 44]. Under this conjecture the free surface deflection equation is obtained:

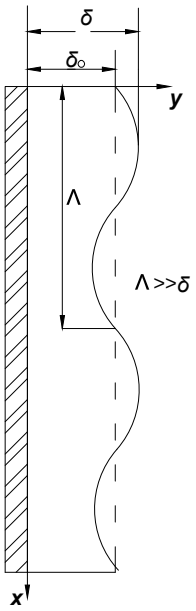


Figure 9: Characteristic dimensions in a Wavy Regime

$$\frac{\psi^3}{We}(1+\phi)^3\frac{\partial^3\phi}{\partial\eta^3} - \left[\frac{Z^2\psi}{5}(1+\phi)^2 - 1.2\psi(1-Z)^2\right]\frac{\partial\phi}{\partial\eta} + Fr(3\phi+3\phi^3+\phi^3) - \frac{12}{Re} + \left[Fr - \frac{12}{Re}\right] = 0 \tag{25}$$

where,

| | | |
|---|---|---|
| Re | = | $\frac{4\Gamma}{\mu}$ |
| We | = | $\frac{\rho U_o^2 \delta o}{\sigma}$ |
| Fr | = | $\frac{g\delta_o}{U_o^2}$ |
| $\eta$ | = | $\frac{x-zt}{\Lambda}$ |
| $Z$ | = | $\frac{z}{U_o}$ |
| $\psi$ | = | $\frac{\delta_o}{\Lambda}$ |

Equation (25) is a nonlinear partial differential equation. Its solution yields in a nondimensional wave profile. Since $\psi$ and $Z$ are variables which are characterized by fluid hydrodynamics and surface tension, then $Z = f(Re, \gamma)$ and $\psi = f(Re, \gamma)$, where $\gamma$ is a nondimensional parameter for the surface tension, and it is defined as $\gamma = \frac{\sigma(\nu^4 g)^{-\frac{1}{3}}}{\rho_l}$. Pierson and Whitaker [40], Anshus [46] have studied and solved the linear stability problem associated a vertical liquid film under the action of gravity in terms of the Orr-Sommerfeld Equation (OSE). OSE describes the linear two-dimensional modes of disturbance to a viscous parallel flow, and it determines with accuracy what the conditions for hydrodynamic stability are. In the case of the free surface flows, the resolution of the OSE provides the characteristic physical parameters of the wave flow ($\psi$ and $Z$). Such parameters are applied in equation (25). Thus, $\psi$ and $Z$ are maintained constant for each solution. The equation (25) can be solved via a numerical spectral method [47]. Therefore, it can be expressed by means of analysis in the Fourier series:

$$\phi(\eta_i) = \sum_{n=1}^{N} A_n sin(2n\pi\eta_i) + B_n cos(2n\pi\eta_i) \tag{26}$$

Equation 26 satisfies the periodical conditions of (25), and both are a mathematical closure problem. The solution is achieved using a $LU$ decomposition to obtain $A_n$ and $B_n$ constants. Thus, $\phi$ and its derivatives can be obtained directly. Therefore, the Gauss-Seidel method is employed to handle nonlinearity.

*3.3. Coolant fluid domain*

The coolant water in counter flow is solved numerically in a step-by step procedure by dividing the domain in concatenated control volumes where the governing equations (conservation of mass, momentum and energy) are applied [48, 49]. At each control volume, the fluid formulation requires the use of the following empirical information: i) the friction factor ($f_i$) [50], to evaluate the averaged shear stress between fluid and solid surface; ii) the heat transfer coefficient ($\alpha_i$) [51], to evaluate the heat transfer between tube and fluid. Finally, the axial temperature field of the tube wall is obtained by integrating and discretizing energy equation which is solved using a TDMA solver [52].

## 4. Global Numerical resolution

Three different domains can be distinguished, see Fig.10: i) the $LiBr - H_2O$ liquid falling film solution; ii) the coolant fluid domain; and iii) the wall tube (solid). Every domain is discretized and is solved independently. In the case of fluid domain the resolution is in flow direction (step-by-step resolution algorithm). In both fluid domains (i) and (ii) the interchange of information goes through the solid domain (iii). The complete resolution is achieved when the temperature field in the wall tube does not undergo changes in its value between consecutive iterations. The kinematic condition in the liquid - vapour interface is satisfied by calculating by means of these two steps: i) the $v$ component of the velocity is calculated by using the mass conservation equation (with constant density) in the curvilinear mesh, from the wall to the interface; ii) the thickness of the falling film is recalculated by assuring mass conservation between two consecutive row nodes (after applying the Free Surface Deflection Equation). The full algorithm resolution is as follows:

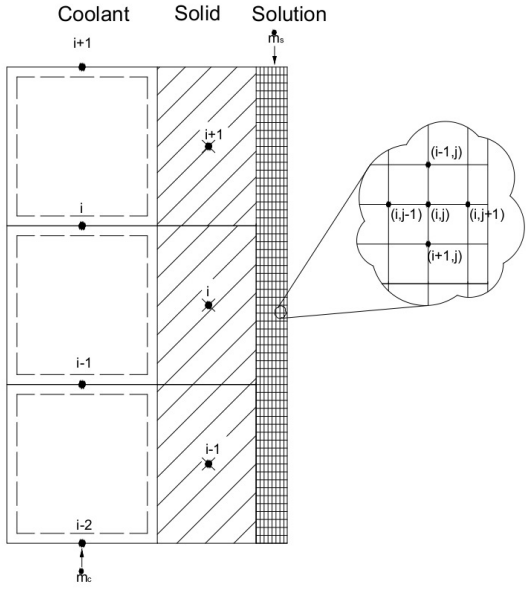


Figure 10: Discretization of $LiBr$ solution, solid and coolant domains (from right to left).

- Falling film domain:

1. Coupled resolution of momentum (16) and mass conservation (15) equations, for obtaining the values of the components of the velocity. Calculation of the boundary layer thickness considering a smooth film thickness.
2. The Free Surface Deflection Equation (25) is solved in order to obtain a wave profile which is function $Re$, and the dimensionless surface tension parameter $\gamma$. The new boundary layer thickness as function of wave profile is calculated and introduced.
3. Coupled resolution of energy (17) and mass species conservation (18) equations.
4. Calculation of the mass absorbed by solving equations: (22), (23) and (24).
5. Check if energy balance at interface is accomplished, $-\lambda \nabla T \cdot \vec{n} = h_{abs} \dot{m}_{abs_v} + h_l \dot{m}_{abs_l}$. If so, continue with the calculation, if not back to point 3.
6. Check if mass balance is accomplished $|\frac{\dot{m}_{abs} - \dot{m}_{abs_o}}{\dot{m}_{abs}}| \leq \varepsilon$. If so, go to the next row, if not, back to point 1.
7. Verification if we are in the last row. If not, next row and, go to point 1. If so, finish.

- Coolant fluid domain:

1. Calculation of fluid properties ($\rho, \mu, h \ldots, etc.$) in function $T_c$ and $P_c$.
2. Resolution of the mass conservation equation.
3. Resolution of the momentum conservation equation in order to obtain $P_i$. Factor friction is obtained using empirical correlations [53].
4. Resolution of the energy conservation equation in order to get $T_i$. The heat transfer coefficients is obtained using empirical correlations [51].
5. Check if mass and energy balances are accomplished. If so, go to the next control volume. If not, back to point 2.
6. Verification if we are in the last control volume. If not, next point and go to point 1. If so, finish.

- Wall tube:

    1. Solve energy conservation equation in order to obtain field temperature along the wall tube $Tw$ ($\forall$ i).
    2. Evaluate $|\frac{T_w - T_w^o}{T_w}| \leq \varepsilon$. If the previous condition is not fulfilled back to calculating falling film domain.

## 5. Results and Discussion

This section presents the experimental studies which were used for the model validation taking into account the presence of "mist flow" together with a comparison with previously published data.

The experimental results presented in this section were obtained by performing a parametric study.

The influence of the principal variables which determine the absorption performance were evaluated.

Most of the experimental points have been obtained free of mist flow except inlet mas flow and inlet $LiBr$ concentrations studies (mist flow is present when $Re > 150$, as explaned in section 2.3).

The variables which have been considered are as follows:

- The influence of the inlet mass flow ($\dot{m}_{l,in}$). Since the rest of the inlet condition remains constant, the $Re$ number changes as $\dot{m}_{l,in}$. During this test the behaviour of the mist flow can be appreciated.

- The influence of absorption pressure ($P_{abs}$). It is controlled through the generation process. This test is free of mist flow since $Re \approx 100$.

- The influence of the inlet solution concentration ($T_{l,in}$). Two different test have been performed at different Reynolds numbers. $Re \approx 250$ (mist flow is present) and $Re \approx 140$ (free of mist flow).

- The influence of the inlet coolant solution ($T_{c,in}$). This test is performed using $Re \approx 115$ ( free of mist flow).

- The influence of the inlet mass concentration ($c_{l,in}$). This tests is performed using $Re \approx 120$ ( free of mist flow).

- A final set of experimental data has been obtained at different $Re = 90 \div 200$ number, and different inlet mass concentration $c_{l,in} = 57.3\% \div 61\%$. This data were used in order to perform the fully validation of the numerical models. Mist flow was present when $Re > 150$.

*5.1. Comparison with other authors*

In this subsection, a comparison with results by other researchers has been performed. In the literature there are not many papers which can be used. An exhaustive study was conducted in order to determine which information was more feasible to reproduce. The selected bibliography is as follows Medrano [24],Miller [23], Yuksel and Schlunder [25] and Takamatsu et al. [12].

In order to make the data comparable, they have been adimensionalized. We use the same dimensionless data reduction as Yuksel and Schlunder [25]. They approach the heat transfer phenomena by an overall comparison of the mean $Nu$ values against $Re$ Number (see Fig. 11). The Nu has been calculated using inlet film properties values ($T_{l,in}$, $c_{l,in}$). The film heat transfer coefficient in equation 28 has been calculated using $U$ values obtained from logarithm mean temperature differences, and the measured temperatures at the inlet and outlet solution conditions.

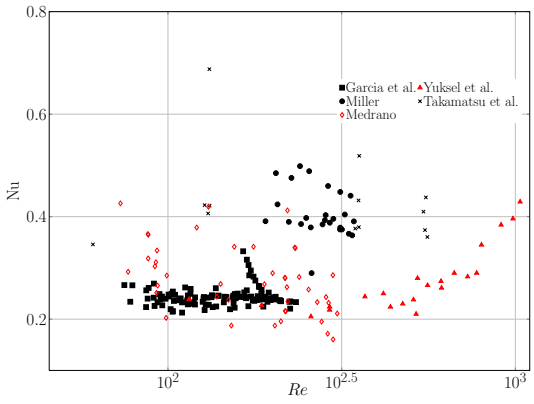


Figure 11: Comparison of experimental $Nu$ number.

It can be observed that the data by Medrano [24] and Takamatsu et al. [12] are more dispersed. In both works, only the points with similar mass transfer

potential with the present research have been chosen for the comparison. On the othe hand, the data by Miller [23] slighthly overestimates the Nu values. In general, the points in the present research are not dispersed and are in agreement with Yuksel and Schlunder [25]. At $Re \approx 180$ there are some dispersed points, this set of points correspond to a degree subcooling inlet temperature.

Concerning the mass transfer, Figure 12 shows the comparison of $Sh$ number vs $Re$. To calculate the $Sh$ number, according to Yuksel and Schlunder [25]. The mean mass transfer coefficient is calculated in the following way:

$$\beta = \frac{\dot{m}_{l,in}}{\rho\pi\ d\ \int_0^L ln\ \frac{(1-c_b)}{1-c_{eq}(T_b,P_{abs})}\ dx} \tag{27}$$

The overall falling film heat transport coefficient according to [25] is calculated as follows:

$$\alpha_s = \left(\frac{1}{U} - \frac{d_{ext}}{2\lambda_{tube}} ln \frac{d_{ext}}{d_{int}} - \frac{d_{ext}}{d_{int}} \frac{1}{\alpha_c}\right)^{-1} \tag{28}$$

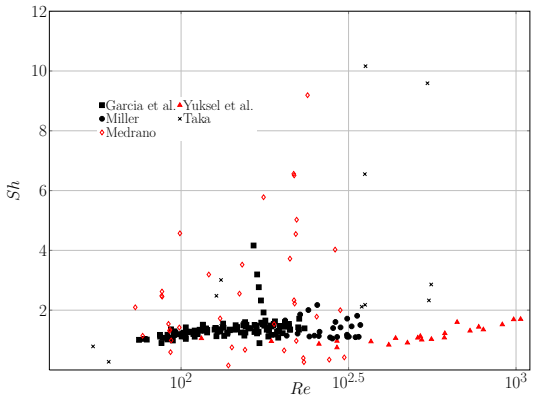


Figure 12: Comparison of experimental $Sh$ number.

Once again, the results agree very well with the ones by Yuksel and Schlunder [25] and Miller [23]. The points of Medrano [24]. and Takamatsu

et al. [12] are more dispersed. We have to point out two aspects in these two works: i) the high degree of subcooling in most of the experimental points; ii) the experimental value of the outlet solution concentration is not taken into account, instead the authors recalculate the outlet concentration value in a iterative procedure.

### *5.2. Falling film mass flow rate effect*

In order to evaluate the effects of the mass flow of solution in the absorption performance the rest of influential variables have been set as follows: $T_{l,in} = T_{l,sat}$, $P_{abs} = 1300$ Pa, $c_{in} = 60.3\%$, $T_{c,in} = 32.5^{o}C$. Relatively high inlet coolant temperatures are selected in order to simulate air-cooled thermal conditions. The coolant mass flow rate ($\dot{m}_{c,in}$) is large enough to provide enough cooling capacity.

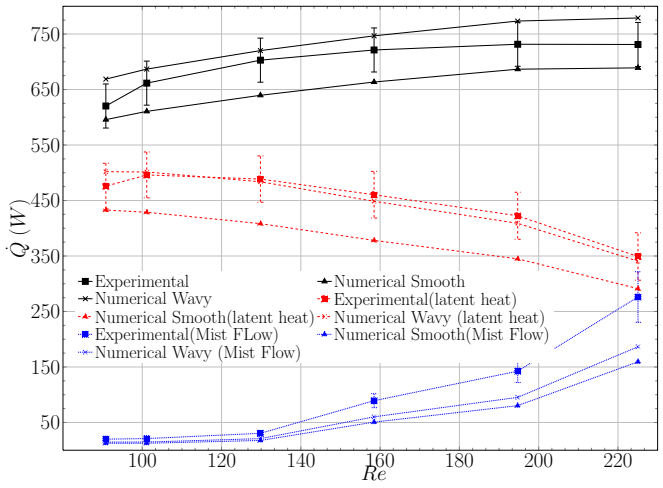


Figure 13: Effects of the inlet mass flow rate ($\dot{m}_{l,in}$) in heat load ($\dot{Q}_{abs,c}$, black dots), energy input through the interface ($\dot{Q}_{abs,v}$, red dots), and enthalpy contribution of mist flow ($\dot{Q}_{abs,l}$, blue dots) transfer rates. Experimental and numerical results (smooth and wavy models).

The Reynolds number in the falling film is manipulated by increasing or decreasing the inlet mass flow. This work presents $Re$ numbers between $90-250$, which are the expected values in absorption machines. $Re$ influence on heat and mass transfer rates are shown in Fig.13 and Fig.14, respectively.

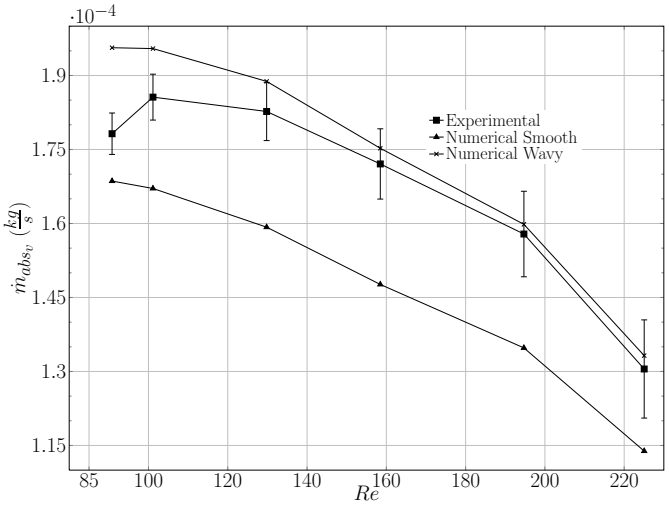


Figure 14: Effects of inlet solution mass flow rate ($\dot{m}_{l,in}$) in the mass of absorption transfer rate ($\dot{m}_{abs,l}$). Experimental and numerical results (smooth and wavy models).

The graph in Fig.14 represents the influence of $Re$ number in the mass absorption rate. Experimentally the mass absorbed presents its maximum value at $Re \approx 100$. From this point, the higher the Re is, the less the mass absorbed. Numerical results present similar tendency. The wavy numerical model matches better than the smooth model. Other experimental investigations [25-27] show that increasing slope reaches its maximum value about $Re \approx 70$ in a range of $Re = 15 \div 100$.

The graph in Fig.13 represents the influence of Re number in heat rate of absorption. The graph represents the following results:

1. The heat contribution due to mist flow ($\dot{Q}_{abs,l}$) increases with $Re$ number (see section 2.3). While the $Re$ values are between $160 - 240$, the two numerical models underestimate the experimental data. However, since $Re \approx 130$ numerical and experimental results match very well.

2. Energy input through the interface in the film interface side ($\dot{Q}_{abs,v}$) decreases as $Re$ increases, and it presents its maximum value when $Re \approx 100$ (this heat contribution depends directly from the mass absorbed). The wavy model matches with experimental data while smooth model results are below the experimental data.

3. The heat load removed directly for the coolant fluid ($\dot{Q}_{abs,c}$) increases as $Re$ increases while $Re = 90 \div 160$, from values about $Re \approx 160$ heat load keeps almost constant. This is due to heat contribution of the mist flow. The wavy model slightly overestimates experimental results, while smooth model results are below the experimental data.

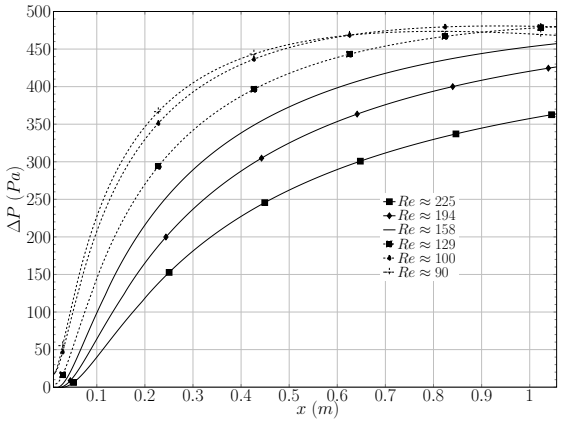


Figure 15: Numerical results of pressure Driving Potential ($\Delta P$) evolution along falling film at different $Re$ number.

The above results show that there is an optimal Reynolds number where heat and mass transfer rates are maximum. Higher values of $Re$ than the optimal, entails in a decrement in absorption performance. In order to explain this phenomena, a numerical study is presented in Fig. 15.

Fig. 15 represents the pressure driving potentials along the falling film. The driving potentials decreases as the $Re$ increases. The trend changes when $Re \approx 90 \div 100$ when both graphs intersect each other. Increasing the $Re$ number, increases the interface velocity of the film. As a consequence, there is a reduction in the exposure time between liquid film and gas phase, and a decrease of the vapour absorption. This fact agrees with the penetration theory [54], which states that the mass transfer coefficient is directly inversely proportional to the exposure time.

### *5.3. Absorption pressure effects*

The driving force for mass transfer through the vapour-liquid interface can be expressed as the difference between the partial pressure of water

vapour in the vapour side of the interface (the gas phase is composed of water vapour and an unknown amount of non-absorbable gases), and the equilibrium pressure in the bulk solution at the given temperature and concentration $P_{l,b} = f(T_{l,b}, c_{l,b})$. If it is assumed that there is no presence of non-absorbable gases, the pressure vapour keeps constant along to all the vapour domain (bulk and interface vapour sides). Thus, the pressure driving force can be expressed by,

$$\Delta P = P_{abs} - P_{l,b} \tag{29}$$

The second term of the right hand side of the equation (29) ($P_{l,b}$) varies its value along the falling film. Therefore, the higher the absorption pressure is, the greater the potential for vapour transfer to the falling film.

The following conditions are fixed $T_{s,in} \approx T_{sat}$, $Re \approx 100$, $c_{in} = 57.3\%$, $T_c \approx 32°C$. The absorption pressure ($P_{abs}$) varies from 850 to 1260 Pa. These tests were free of mist flow ($Re < 150$). Fig. 16 shows the influence of absorption pressure in the heat load rates ($\dot{Q}_{abs,c}$), and the energy input through the interface ($\dot{Q}_{abs,v}$).

There was an increment in the values of $\dot{Q}_{abs,c}$ from 224 to 438 $W$ (95%), and a increment in the values of $\dot{Q}_{abs,v}$ from 165 to 355 $W$ (115%). On the other hand, Fig. 17 represents the influence of absorption pressure in the mass transfer rates ($\dot{m}_{abs,v}$). As expected, the flux mass has the same tendency as the energy input through the interface. Both Numerical models follow the same behaviour as experimental data. The wavy model tends to over-predict the experimental data in this test. (between $8 - 16\%$ in $\dot{Q}_{abs,c}$ and $8 - 22\%$ for $\dot{Q}_{abs,v}$).

### *5.4. Inlet solution temperature effects*

All experimental tests were performed by approximating the inlet solution temperature to the equilibrium conditions ($T_{l,in} \approx T_{sat}$). Theoretically, any variation above or below (subcooling or superheating) from equilibrium conditions should be reflected in the performance of the absorber. In this section, the subcooling effects have been taken into account. During the absorption process in a falling film, it is assumed that the interface liquid-vapour is under equilibrium conditions. It means that $LiBr$ concentration and temperature at the interface are such that the vapour pressure of water

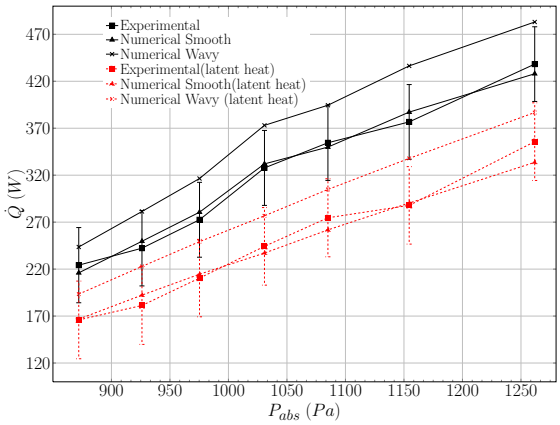


Figure 16: Influence of absorption pressure ($P_{abs}$) in both heat load ($\dot{Q}_{abs,c}$, black dots) and energy input through the interface ($\dot{Q}_{abs,v}$, red dots) transfer rates. Experimental and numerical results (smooth and wavy models).

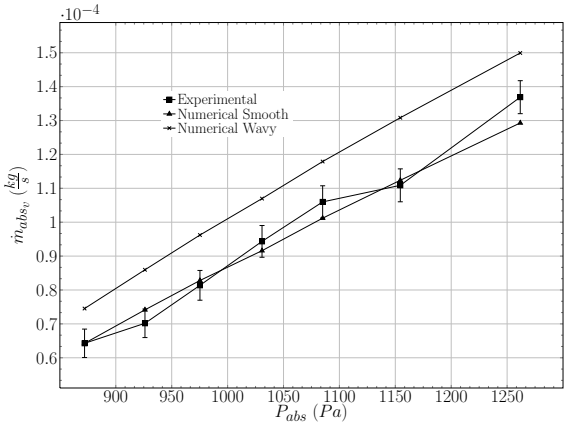


Figure 17: Influence of the absorption pressure ($P_{abs}$) in the mass of absorption transfer rate ($\dot{m}_{abs,v}$). Experimental and numerical results (smooth and wavy models)

in the solution is always equal to the partial pressure of $H_2O$ vapour in the vapour phase. When the inlet temperature solution is approximately equal to the saturation temperature ($T_{l,in} \approx T_{sat}$), equilibrium conditions at the interface are reached early. In contrast, when there is a subcooling degree, there is a process of reaching equilibrium that promotes the absorption of water vapour into the liquid interface.

Fig. 18 and the Fig. 19 depict experimental and numerical results in the heat and mass transfer rates under the influence of subcooling effects. Both graphs show a marked improvement in the absorption process: the mass and heat absorbed present about 20% of increment. The heat load shows an opposite trend; it decreases as $T_{l,in}$ decreases. This is due to the fact that the greater the subcooling degree is, the less the sensible heat in the liquid which is entering in the absorber. In spite of the increase of energy input through the interface, this is not large enough to revert this tendency.

Nevertheless, Fig. 20 and Fig. 21 describe a different behaviour when a subcooling grade is manipulated. It is also interesting to point out that the numerical results also predict this behaviour. The only difference between both tests is the Re number ($Re \approx 200$ for Fig. 18, and $Re \approx 140$ for Fig. 20). However, the experimental data with $Re > 150$ has presence of mist flow. This fact could give an erratic interpretation of the results. In other words, the enhancement of the absorption process could be due to the presence of mist flow, rather than an increment of $Re$. The numerical results also predict this behaviour.

In order to solve this ambiguity, a numerical study is performed. Fig. 22 and Fig. 23 depict numerical simulations under the influence of subcooling, in a range of $Re$ and non-presence of mist flow. The results of the numerical study show that the influence of the subcooling is conditioned by the regime flow. Flow regimes between $Re \div 70 - 140$ show a negative tendency when increasing the subcooling degree, this is not only useless for the enhancement of the absorption rates, but it also seems to degrade the absorption performance. Such tendency is reverted starting from $Re > 140$. From this point, subcooling has a positive influence in the absorption rates.

At high Re numbers the effect of subcooling is favourable to mass transfer, because the thermal boundary layer of the interface does not reach the thermal boundary layer of the wall. At low Re numbers the two thermal boundary layers contact, and the overall effect is that part the heat of absorption is used for heating the falling film. There is a transfer of some absorption heat in sensible heat to the film, not to the wall.

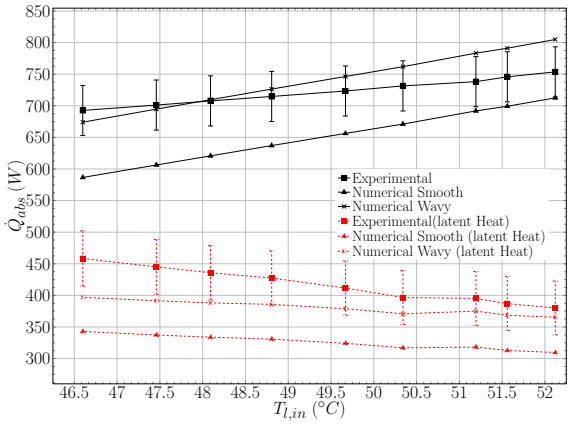


Figure 18: Influence of the inlet solution temperature ($T_{l,in}$) in both heat load ($\dot{Q}_{abs,c}$, black dots), and energy input through the interface ($\dot{Q}_{abs,v}$, red dots) transfer rates for $Re \approx 250$. Experimental and numerical results (smooth and wavy models).

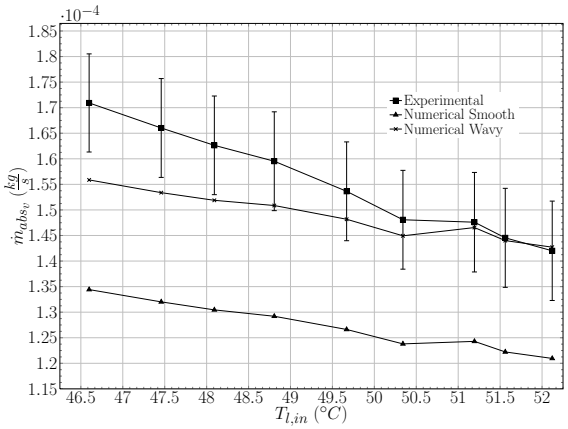


Figure 19: Influence of inlet solution temperature ($T_{l,in}$) in the mass absorption transfer rate ($\dot{m}_{abs,v}$) for $Re \approx 250$. Experimental and numerical results (smooth and wavy models).

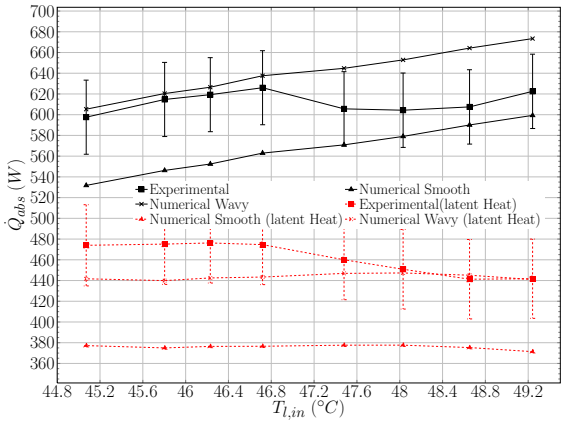


Figure 20: Influence of the inlet solution temperature ($T_{l,in}$) in both heat load ($\dot{Q}_{abs,c}$, black dots) and energy input through the interface ($\dot{Q}_{abs,v}$, red dots) transfer rates for $Re \approx 140$. Experimental and numerical results (smooth and wavy models).

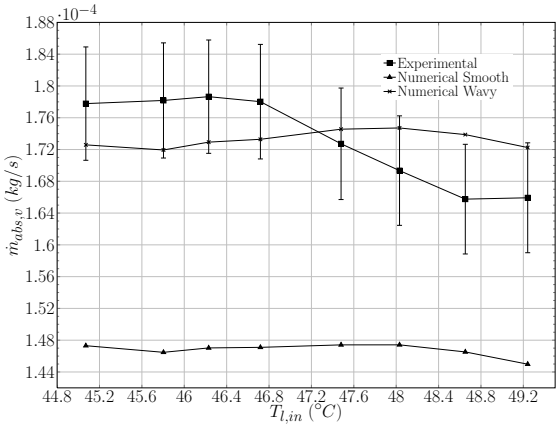


Figure 21: Influence of the inlet solution temperature ($T_{l,in}$) in the mass absorption transfer rate ($\dot{m}_{abs,v}$) for $Re \approx 140$. Experimental and numerical results (smooth and wavy models).

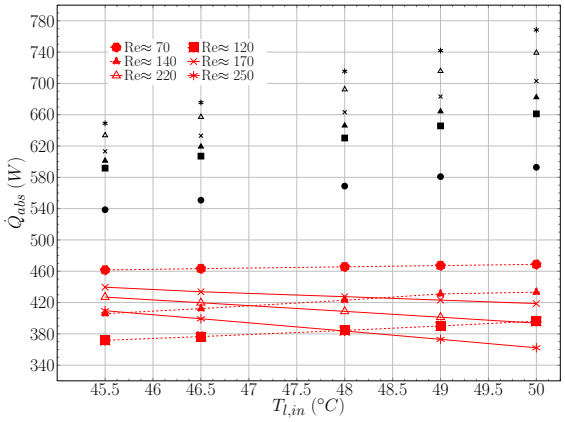


Figure 22: Numerical study of the influence of the inlet solution temperature $(Tl, in)$ in both heat load ($\dot{Q}_{abs,c}$, black dots), and energy input through the interface ($\dot{Q}_{abs,v}$, red dots) transfer rates at different flow regimes.

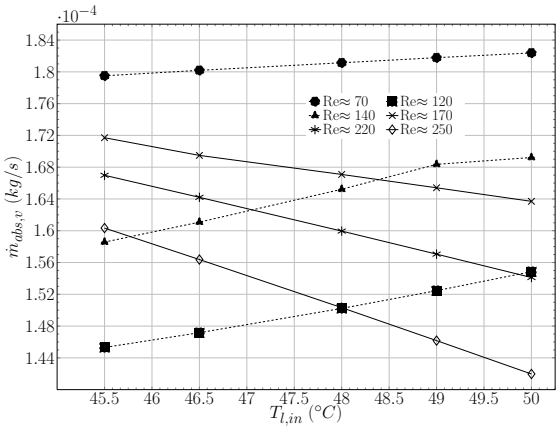


Figure 23: Numerical study of the influence of the inlet solution temperature $(Tl, in)$ in mass absorption rates ($\dot{m}_{abs,v}$) at different flow regimes.

### 5.5. *Inlet coolant temperature effects*

The variables used for evaluating coolant temperature effects are: $P_{abs} \approx 1200$ Pa, $Re \approx 115$, $c_{l,in} \approx 59.50\%$, $T_{c,in} \approx 30.1 - 41.7°C$. Fig. 24 shows the behaviour of both the heat load ($\dot{Q}_{abs,c}$) and the energy input through the interface ($\dot{Q}_{abs,v}$): when the value of $T_{c,in}$ decreases the values of $\dot{Q}_{abs,c}$ and $\dot{Q}_{abs,v}$ increase. The mass transfer rates ($\dot{m}_{abs,v}$) exhibit the same tendency of the energy input through the interface (see Fig. 25). It increases its value as $T_{c_{in}}$ decreases. The agreement between experimental data and numerical results is quite acceptable. However, numerical results of the wavy model show a better matching.

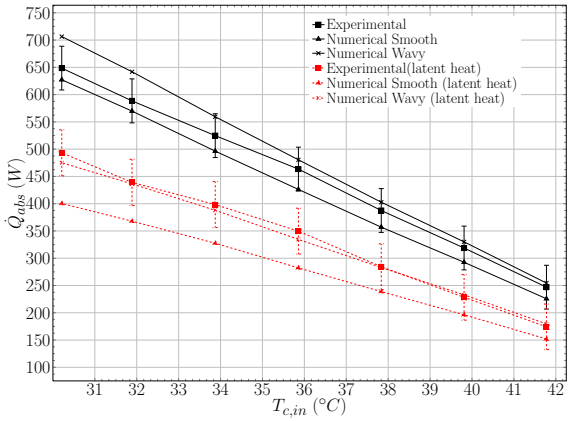


Figure 24: Influence of the inlet coolant temperature ($T_{c,in}$) in both heat load ($\dot{Q}_{abs,c}$, black dots), and energy input through the interface ($\dot{Q}_{abs,v}$, red dots) transfer rates. Experimental and numerical results (smooth and wavy models).

### 5.6. *Mass concentration effects*

The mass concentration is a variable that cannot be directly settled in an absorption machine, but it is settled as a consequence of the equilibrium and performance of the rest of the components. The variables used for evaluating coolant temperature effects are: $P_{abs} \approx 1300$ Pa, $Re \approx 125$, $T_{c,in} \approx 30.0°C$.

The variation of the inlet solution concentration ($c_{l,in}$) and its impact to the mass and the heat transfer rates, respectively, are shown in Fig. 26 and Fig. 27. When increasing concentration in a mixture, the equilibrium pressure decreases, which produces higher driving absorption potential. As

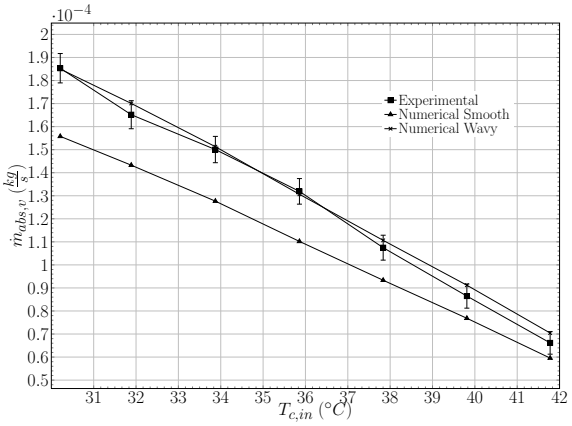


Figure 25: Influence of the inlet coolant temperature ($T_{c,in}$) in the mass absorption transfer rate ($\dot{m}_{abs,v}$). Experimental and numerical results (smooth and wavy models).

expected, the higher the inlet mass concentration is, both mass absorbed ($\dot{m}_{abs}$) and heat load ($\dot{Q}_{abs,c}$) increase.

### *5.7. Experimental Results for the Fully Validation of the Numerical Model*

In the above subsections 5.2-5.6, all the experimental results have been carefully performed in order to obtain vapour water with no presence of mist flow (when it was possible). However, the mathematical model described in section 3.1 has been modified in order to consider the presence of mist flow. An additional set of experimental tests has been carried out under a wide range of flow regimes $Re \approx 70 \div 250$, and concentrations $c_{l,in} \approx 57 - 61\%$ $LiBr$ which were not free of mist flow.

Fig. 28 shows the comparison of the heat load ($\dot{Q}_{abs,c}$) between experimental data and numerical results (wavy and smooth models). The red errors lines represent the maximum error calculated in the uncertainty analysis ($\pm 8\%$). However, not all the points are inside this range of errors. The blue error lines represent the maximum discrepancy between experimental and numerical wavy model ($\pm 14\%$). The experimental data compared against the wavy mathematical model shows the following discrepancies: maximum 14%, minimum 0.490% and average 6.68%. In contrast, the smooth model shows the following discrepancies: maximum 11.12%, minimum 0.3% and average 5.29%.

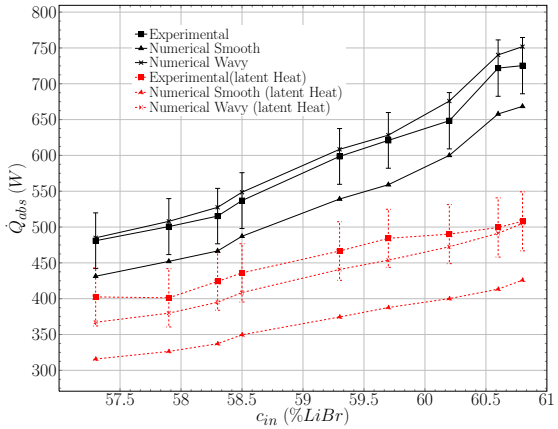


Figure 26: Influence of the inlet solution concentration ($c_{l,in}$) in both heat load ($\dot{Q}_{abs,c}$, black dots), and energy input through the interface ($\dot{Q}_{abs,v}$, red dots) transfer rates. Experimental and numerical results (smooth and wavy models).

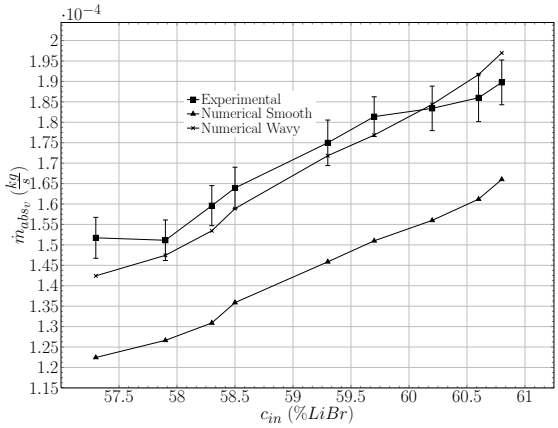


Figure 27: Influence of the inlet solution concentration ($c_{l,in}$) in the mass absorption transfer rate ($\dot{m}_{abs,l}$). Experimental and numerical results (smooth and wavy models).

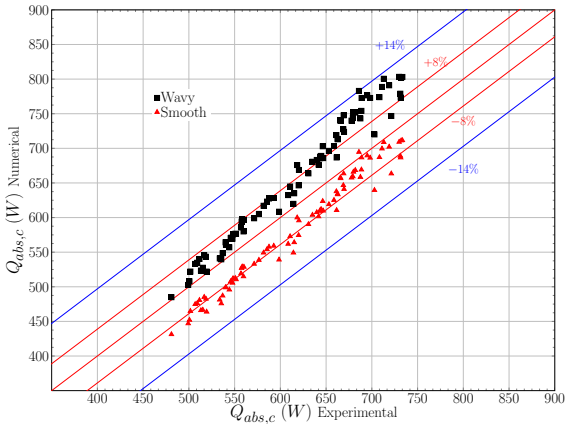


Figure 28: Comparison of the heat load ($\dot{Q}_{abs,c}$) between numerical and experimental results at different flow regimes and different inlet solution mass concentration (red dots refers smooth model, black dots refers to wavy model).

Fig. 29 shows the comparison between experimental and numerical results obtained from the mathematical models corresponding to the water vapour mass absorbed ($\dot{m}_{abs,v}$). The maximum error associated with uncertainty analysis is ($\pm$11.5%). Most of the wavy numerical data are inside this range of error. The experimental data compared against the wavy mathematical model shows the following discrepancies: maximum 15.15%, minimum 0.05% and average 5.43%. In contrast, the smooth model shows the following discrepancies: maximum 22.21%, minimum 3.0% and average 13.66%.

The wavy regime improves the mass transfer due to the effect of mixing of the additional movement. The smooth model cannot anticipate this effect, that this specially important in the mass absorbed prediction.

## 6. Conclusions and Future Work

### *6.1. Experimental work*

The following conclusions during the experimental procedures are highlighted:

- An unexpected condition has been detected during the experimental performance, the presence of micro-droplets which are entrained by the water vapour during the generation process. The mist flow increases

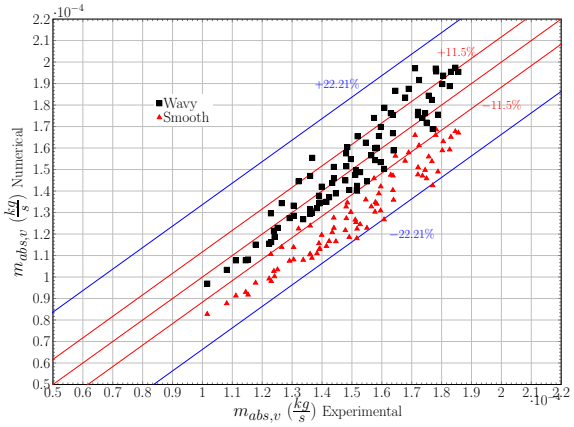


Figure 29: Comparison of the mass absorbed ($\dot{m}_{abs,v}$) between numerical and experimental results at different flow regimes and different inlet solution mass concentration ($c_{l,in}$) (red dots refers smooth model, black dots refers to wavy model).

as the $Re$ number increases. We consider that the vapour mass flow is free of mist flow when $Re \leq 150$. In spite of the efforts to reduce such phenomena, it was not possible to obtain unpolluted water vapour from the generator. However, it has been possible to evaluate indirectly the quantity of mist-flow which leaks into the absorber in the form of the global void fraction.

- The principal cause of mist flow generation is the way heat is applied to the generator. In this experiment, two ways have been used in order to apply the heat to the generator: i) an immersion electrical heater; ii) a set of flexible silicone rubber heaters placed directly on the outer surface of the generator. It causes high heat fluxes per unit of area ($W \cdot m^{-2}$). As a consequence, high vapour velocities are provoked [55] and, thus a big amount of nucleated boiling is provoked. The high velocities in the vapour conductions drag the drops produced and, consequently, this is probably the origin of the mist flow.

### *6.2. Validation of the Mathematical Models*

A parametric study has been carried out in order to evaluate the principal working conditions that drive the absorption phenomena in vertical absorbers. The main conclusions are:

- The study of the influence of inlet mass flow solution demonstrates there is an $Re$ number where the absorber performance is optimal ($Re \approx 100$). The reason of the fact $Re > 100$ decreases the absorption performance is due to the reduction of the exposure time between the liquid film and vapour phase. For instance, according to the penetration theory [54, 56], the mass transfer coefficient is directly proportional to this exposure time. Numerical studies reproduce this condition, showing that driving potentials reduce when $Re > 100$.

- Experimental results show an improvement of up to 115% when the absorption pressure increases from $P_{abs} = 850$ Pa to $P_{abs} = 1300$ Pa. Both mathematical models (laminar smooth and laminar wavy) show the same behaviour.

- The influence of $T_{l,in}$ is conditioned to the flow regime. For $Re < 140$ the subcooling has negative influence in the absorber, conversely subcooling degree seems to be a positive trending when $Re > 140$. It shows an improvement of about 20% when the subcooling degree is about 5.6° C.

- The heat and mass transfer rates increases as the inlet coolant temperature $T_{c,in}$ decreases: the heat and mass transfer rates 177% and 172%, respectively, when the value of inlet coolant temperature decreases from $T_{c,in} \approx 42°C$ to $T_{c,in} \approx 30°C$.

- When the inlet mass fraction $c_{in}$ increases its value, the pressure driving potential increases. Therefore, the absorption performance shows an improvement in the heat absorbed 25% and of mass transfer of 23%, when the value of inlet mass concentration increases from $c_{in} \approx 57.25\%wt$ to $c_{in} \approx 60.75\%$. Other important aspects to be highlighted is the fact that values higher than $c_{l,in} > 61\%$ causes crystallization problems.

- The laminar wavy model shows a better agreement with the experiments than the laminar smooth model in the predictions of the mass transfer rates $m_{abs,v}$. For the heat load $Q_{abs,c}$, both models exhibit a similar performance.

*6.3. Future Work*

In order to improve the experimental set-up, a definitive solution for eradicating the mist flow must involve the redesigning of the generator. To increase the heat transfer area, possible solutions could be a generator using a flooded finned-tube heat exchanger endowed with a recirculation system in order to avoid nucleation, or a falling film generator operated by a secondary fluid as a source of heat.

## 7. Acknowledgments

This research has been financed and supported by the Spanish Government through the project "Simulación numérica y validación experimental de fenómenos de cambio de fase líquido-vapour. Aplicación a sistemas y equipos térmicos (II) (Ref. ENE2011-28699)" and by the EIT through KIC Innoenergy (Energy Storage project).

# Nomenclature

| | |
|---|---|
| $A_n, B_n$ | coefficients in Fourier series |
| $a$ | thermal diffusivity, $m^2\ s^{-1}$ |
| $c_p$ | specific heat capacity, $J\ kg^{-1}\ K^{-1}$ |
| $c$ | $LiBr$ mass fraction concentration |
| $d$ | diameter of the absorber |
| $D$ | mass diffusivity, $m^2\ s^{-1}$ |
| $f$ | friction factor |
| $g$ | acceleration due to gravity, $m\ s^{-2}$ |
| $h$ | specific enthalpy, $J\ kg^{-1}$ |
| $L$ | absorber length $m$ |
| $\dot{m}$ | mass flow , $kg\ s^{-1}$ |
| $\vec{n}$ | unitary normal vector |
| $P$ | pressure, $Pa$ |
| $\dot{Q}$ | heat rate, $W$ |
| $T$ | temperature, $K$ |
| $t$ | time, $s$ |
| $U$ | overall heat transfer coefficient, $W\ m^{-2}\ K^{-1}$ |
| $U_o$ | mean characteristic velocity, $m\ s^{-1}$ |
| $u$ | velocity profile x axis direction, $m\ s^{-1}$ |

| | |
|---|---|
| $v$ | velocity profile y axis direction, $m\ s^{-1}$ |
| $X$ | void fraction |
| $x$ | coordinate, $m$ |
| $y$ | coordinate, $m$ |
| $z$ | wave velocity, $m\ s^{-1}$ |
| $Z$ | dimensionless Wave velocity |

**Greek symbols**

| | |
|---|---|
| $\alpha$ | heat transfer coefficient, $W\ m^{-2}\ K^{-1}$ |
| $\beta$ | mass transfer coefficient, $m\ s^{-1}$ |
| $\delta$ | film thickness, $m$ |
| $\delta_o$ | mean film thickness, $m$ |
| $\Gamma$ | mass flow rate per unit length, $kg\ s^{-1}\ m^{-1}$ |
| $\gamma$ | nondimensional parameter for the surface tension |
| $\eta$ | dimensionless x coordinate in wave profile |
| $\varepsilon$ | convergence accuracy criterion |
| $\theta$ | inclination angle, $rad$ |
| $\mu$ | dynamic viscosity, $kg\ m^{-1}\ s^{-1}$ |
| $\nu$ | kinematic viscosity, $m^2\ s^{-1}$ |
| $\Lambda$ | wave length, $m$ |
| $\lambda$ | thermal conductivity, $W\ m^{-1}\ K^{-1}$ |
| $\rho$ | density, $kg\ m^{-3}$ |
| $\tau$ | tangential coordinate in free surface, $m$ |
| $\phi$ | dimensionless y coordinate in wave profile |
| $\sigma$ | surface tension, $N\ m^{-1}$ |
| $\psi$ | wave number |
| $\xi$ | Dimensionless $x$ coordinate |

**Dimensionless Groups**

| | |
|---|---|
| $Fr$ | Froude Number, $Fr = \frac{g\delta_o}{V_o^2}$ |
| $Nu$ | Nusselt film Number, $\alpha(\nu^2/g)^{1/3}/\lambda$ |
| $Re$ | Reynolds Number, $Re = \frac{4\Gamma}{\mu}$ |
| $Sh$ | Sherwood Numbe,r $\beta(\nu^2/g)^{1/3}/D$ |
| $We$ | Weber Number, $We = \frac{\rho V_o^2 \delta_o}{\sigma}$ |

**Subscripts**

| | |
|---|---|
| $abs$ | absorption |
| $b$ | bulk |
| $c$ | coolant fluid |
| $eq$ | equilibrium |
| $ext$ | exterior |
| $gen$ | generation process |
| $H_2O$ | related to water element |
| $if$ | interface conditions |
| $i$ | grid position in $x$ direction |
| $in$ | inlet conditions, inner |
| $int$ | interior |
| $l$ | liquid phase in LiBr solution |
| $out$ | outlet conditions, outer |
| $s$ | solution |
| $t$ | total |
| $tube$ | tube |
| $v$ | vapour phase |
| $w$ | wall solid tube |

**Superscripts**

| | |
|---|---|
| $\bar{}$ | arithmetic average |
| $o$ | previous step value |

## Appendix A. Mass Absorption in Presence of Mist Flow

Fig. (A.30) depicts the liquid-vapour interface between the liquid film and the vapour water in presence of mist flow. The total mass that crosses the interface is given by,

$$\dot{m}_t = \dot{m}_{abs,v} + \dot{m}_{abs,l} \tag{A.1}$$

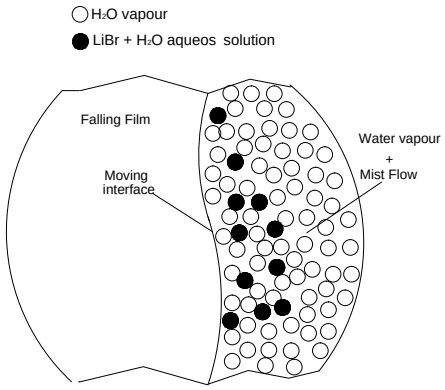


Figure A.30: Schematic description of mist flow in the liquid-vapour interface.

Since our interest is to evaluate the vapour water absorbed, it is more useful to evaluate the total mass of $H_2O$ which is enters into the film,

$$\dot{m}_{abs_{H_2O,t}} = \dot{m}_{abs,v} + \dot{m}_{abs_{H_2O,l}} \tag{A.2}$$

The second term of the left side of the above equation represents the portion of water in the mist flow,

$$\dot{m}_{abs_{H_2O,l}} = \dot{m}_{abs,l}(1 - c_{l,in}) \tag{A.3}$$

where the concentration of mist flow is assumed to be the same as inlet concentration, since the aqueous solution in the generator is homogeneous. In order to close the set equations, an extra equation is still needed.

$$\dot{m}_{abs_{H_2O,t}} = c_{H_2O_{if}}(\dot{m}_{abs_{H_2O,t}} + \dot{m}_{abs_{LiBr,l}}) - D_l\rho_l\nabla c_{H_2O} \cdot \vec{n} \tag{A.4}$$

The above equation represents Fick's law for two inmiscible moving fluids. The term $\dot{m}_{abs_{LiBr,l}}$ represents the portion of $LiBr$ contained in the mist flow. Such term can also be expressed as,

$$\dot{m}_{abs_{LiBr,l}} = \dot{m}_{abs,l} c_{l,in} \tag{A.5}$$

replacing equation (A.5) into equation (A.6) yields,

$$\dot{m}_{abs_{H_2O,t}} = c_{H_2O_{if}} (\dot{m}_{abs_{H_2O,t}} + \dot{m}_{abs,l} c_{in}) - D_l \rho_l \nabla c_{H_2O} \cdot \vec{n} \tag{A.6}$$

developing and regrouping,

$$\dot{m}_{abs_{H_2O,t}} = \frac{c_{H_2O_{if}}}{(1 - c_{H_2O_{if}})} \dot{m}_{abs,l} c_{l,in} - \frac{D_l \rho_l}{(1 - c_{H_2O_{if}})} \nabla c_{H_2O} \cdot \vec{n} \tag{A.7}$$

Equation (A.7) can also be expressed in terms of the $LiBr$ concentration since $c_{H_2O} = 1 - c$,

$$\dot{m}_{abs_{H_2O,t}} = \frac{(1 - c_{l,if}) \dot{m}_{abs,l} c_{l,in}}{c_{l,if}} + \frac{D_l \rho_l}{c_{l,if}} \nabla c \cdot \vec{n} \tag{A.8}$$

Equations (A.2), (A.3) and (A.8) are solved simultaneously in order to evaluate the mass fluxes that enters in the liquid-vapour interface.

## Appendix B. Experimental Data

In this appendix the experimental data that allows to perform the energy and mass balance explained in section 2.1 are presented. Table B.6 shows the inlet and outlet conditions as well as the experimental results for the absorption process at different $Re$ for a typical set of experiments. From the inbalances in equations (1) and (4).

Table B.7 shows the experimental data corresponding to the coolant side.

| $Re$ | Inlet conditions | | | | Outlet conditions | | | Results | | | |
|---|---|---|---|---|---|---|---|---|---|---|---|
| | $\dot{m}_{l,in}$ $(\frac{kg}{s})$ | $T_{l,in}$ $(\cdot C)$ | $c_{l,in}$ | $h_{l,in}$ $(\frac{J}{Kg})$ | $T_{l,out}$ $(\cdot C)$ | $c_{l,out}$ | $h_{l,out}$ $(\frac{J}{Kg})$ | $\dot{Q}_{abs,v}$ $(W)$ | $\dot{Q}_{abs,l}$ $(W)$ | $\dot{m}_{abs,v}$ $(\frac{kg}{s})$ | $\dot{m}_{abs,l}$ $(\frac{kg}{s})$ |
| 225 | 1.696e-02 | 5.172e+01 | 6.026e-01 | 1.419e+05 | 4.450e+01 | 5.984e-01 | 1.259e+05 | 3.491e+02 | 2.761e+02 | 1.305e-04 | 1.207e-03 |
| 194 | 1.468e-02 | 5.187e+01 | 6.030e-01 | 1.424e+05 | 4.419e+01 | 5.969e-01 | 1.245e+05 | 4.224e+02 | 1.424e+02 | 1.578e-04 | 6.200e-04 |
| 158 | 1.199e-02 | 5.188e+01 | 6.034e-01 | 1.426e+05 | 4.365e+01 | 5.952e-01 | 1.226e+05 | 4.603e+02 | 8.930e+01 | 1.720e-04 | 3.891e-04 |
| 129 | 9.850e-03 | 5.181e+01 | 6.039e-01 | 1.427e+05 | 4.306e+01 | 5.930e-01 | 1.204e+05 | 4.908e+02 | 3.045e+01 | 1.835e-04 | 1.332e-04 |
| 100 | 7.666e-03 | 5.150e+01 | 6.041e-01 | 1.422e+05 | 4.226e+01 | 5.898e-01 | 1.173e+05 | 5.028e+02 | 2.131e+01 | 1.881e-04 | 9.407e-05 |
| 89 | 6.894e-03 | 5.147e+01 | 6.041e-01 | 1.421e+05 | 4.207e+01 | 5.889e-01 | 1.165e+05 | 4.814e+02 | 2.019e+01 | 1.802e-04 | 9.014e-05 |

Table B.6: Typical set of experimental data at different $Re$ numbers.



| $Re$ | Inlet conditions | | | Outlet conditions | | Results |
|---|---|---|---|---|---|---|
| | $\dot{m}_{c,in}$ $(\frac{kg}{s})$ | $T_{c,in}$ $(\cdot C)$ | $h_{c,in}$ $(\frac{J}{Kg})$ | $T_{c,out}$ $(\cdot C)$ | $h_{c,out}$ $(\frac{J}{Kg})$ | $\dot{Q}_{abs,c}$ $(W)$ |
| 225 | 0.1186 | 32.8805 | 1.378988e+05 | 34.3579 | 1.440791e+05 | 7.311408e+02 |
| 194 | 0.1184 | 32.8765 | 1.378821e+05 | 34.3574 | 1.440770e+05 | 7.315425e+02 |
| 158 | 0.1185 | 32.8864 | 1.379235e+05 | 34.3441 | 1.440214e+05 | 7.212672e+02 |
| 129 | 0.1186 | 32.8879 | 1.379298e+05 | 34.3078 | 1.438696e+05 | 7.028829e+02 |
| 100 | 0.1185 | 32.888 | 1.379302e+05 | 34.226 | 1.435274e+05 | 6.615037e+02 89 |
| 0.1186 | 32.9028 | 1.379921e+05 | 34.1559 | 1.432342e+05 | 6.202940e+02 | |

Table B.7: Typical set of coolant side experimental data at different $Re$ number.

Listed below are the bibliographical sources from where the thermophysical properties for the $LiBr - H_2O$ are obtained.

- Relation $h_l = f(T_l, c)$ is obtained from Yuan and Herold [57]
- Relation $k_l = f(T_l, c)$ is obtained from DiGuilio et al. [58]
- Relation $\rho_l = f(T_l, c)$ is obtained from Chua et al. [20]
- Relation $\mu_l = f(T_l, c)$ is obtained from Lee et al. [59]
- Relation $_l = f(T_l, c)$ is obtained from Yuan and Herold [57], Kaita [60]
- Relation $T_l = f(P, c)$ is obtained from McNeely [61]

## Appendix C. Influence of the $\rho(c, T)$ function

In this appendix, a comparison between the mass absorbed for a typical series of experiments is shown. Different values are obtained according to the used relation between density, LiBr concentration and temperature. Chua et al. [20] has been taken as reference value. The maximum discrepancies are about 5% for the highest Re value using Lee et al. [59]. Wimby and Berntsson [62] and Patek and Klofar [63] have better matches.

| Author | Inlet conditions | | | Outlet conditions | | Results | |
|---|---|---|---|---|---|---|---|
| | $\dot{m}_{l,in}$ (kg/s) | $c_{l,in}$ (%LiBr) | $T_{l,in}$ ($\cdot C$) | $c_{l,out}$ (w LiBr) | $T_{l,out}$ ($\cdot C$) | $\dot{m}_{abs,l}$ (kg/s) | Discrepancy (%) |
| Chua et al. | 0.6892e-2 | 0.6041 | 51.47 | 0.5880 | 42.07 | 1.8876e-4 | Reference |
| Lee et al. | 0.6892e-2 | 0.6006 | 51.47 | 0.5853 | 42.07 | 1.8093e-4 | -4.16 |
| Wimby et al. | 0.6892e-2 | 0.6041 | 51.47 | 0.5885 | 42.07 | 1.8321e-4 | -2.94 |
| Patek et al. | 0.6892e-2 | 0.6115 | 51.47 | 0.5951 | 42.07 | 1.8987e-4 | 0.59 |
| Chua et al. | 0.7666e-2 | 0.6041 | 51.50 | 0.5898 | 42.26 | 1.8587e-4 | Reference |
| Lee et al. | 0.7666e-2 | 0.6006 | 51.50 | 0.5887 | 42.26 | 1.7802e-4 | -4.22 |
| Wimby et al. | 0.7666e-2 | 0.6041 | 51.50 | 0.5902 | 42.26 | 1.8037e-4 | -2.96 |
| Patek et al. | 0.7666e-2 | 0.6115 | 51.50 | 0.5970 | 42.26 | 1.8670e-4 | 0.45 |
| Chua et al. | 0.9850e-2 | 0.6039 | 51.81 | 0.5930 | 43.06 | 1.8105e-4 | Reference |
| Lee et al. | 0.9850e-2 | 0.6004 | 51.81 | 0.5901 | 43.06 | 1.7316e-4 | -4.36 |
| Wimby et al. | 0.9850e-2 | 0.6039 | 51.81 | 0.5934 | 43.06 | 1.7564e-4 | -2.99 |
| Patek et al. | 0.9850e-2 | 0.6113 | 51.81 | 0.6003 | 43.06 | 1.8155e-4 | 0.27 |
| Chua et al. | 1.1900e-2 | 0.6034 | 51.88 | 0.5952 | 43.65 | 1.6394e-4 | Reference |
| Lee et al. | 1.1900e-2 | 0.6000 | 51.88 | 0.5922 | 43.65 | 1.5644e-4 | -4.58 |
| Wimby et al. | 1.1900e-2 | 0.6034 | 51.88 | 0.5955 | 43.65 | 1.5895e-4 | -3.05 |
| Patek et al. | 1.1900e-2 | 0.6108 | 51.88 | 0.6043 | 43.65 | 1.6389e-4 | -0.04 |
| Chua et al. | 1.4680e-2 | 0.6030 | 51.87 | 0.5969 | 44.19 | 1.5002e-4 | Reference |
| Lee et al. | 1.4680e-2 | 0.5996 | 51.87 | 0.5938 | 44.19 | 1.4272e-4 | -4.86 |
| Wimby et al. | 1.4680e-2 | 0.6030 | 51.87 | 0.5971 | 44.19 | 1.4533e-4 | -3.13 |
| Patek et al. | 1.4680e-2 | 0.6104 | 51.87 | 0.5993 | 44.19 | 1.4938e-4 | -0.43 |
| Chua et al. | 1.6960e-2 | 0.6026 | 51.72 | 0.5984 | 44.50 | 1.1904e-4 | Reference |
| Lee et al. | 1.6960e-2 | 0.5992 | 51.72 | 0.5952 | 44.50 | 1.1257e-4 | -5.43 |
| Wimby et al. | 1.6960e-2 | 0.6027 | 51.72 | 0.5986 | 44.50 | 1.1511e-4 | -3.30 |
| Patek et al. | 1.6960e-2 | 0.6100 | 51.72 | 0.6058 | 44.50 | 1.1746e-4 | -1.32 |

Table C.8: Comparison of the mass absorbed according to different $\rho(C,T)$ relations for a typical run of experiments.

## References


[1] R. Zogg, M. Y. Feng, D. Westphalen, Guide to Developing air-cooled LiBr absorption for light commercial combined heat and power applications., Technical Report, United States Department of Energy, 2005.

[2] T. Ohuchi, M. Aizawa, R. Kawakami, A. Nishiguchi, T. Hatada, Y. Kunugi, A Study on a Hot-Water Driven Air-Cooled Absorption Refrigerating Machine, in: Proceedings of the 1994 International Refrigeration Engineering Conference at Purdue, pp. 275–280.

[3] D. S. Kim, I. Ferreira, Air cooled LiBr water absorption chillers for solar air conditioning in extremely hot weathers., Energy Conversion Management 50 (2007) 1018–1025.

[4] M. Medrano, M. Bourouis, A. Coronas, Absorption of water vapour in the falling film of water-lithium bromide inside a vertical tube at air-cooling thermal conditions, Industrial and Engineering Chemical Fundamentals 31 (2001) 891–898.

[5] N. I. Grigoreva, V. Y. Nakoyarkov, Exact Solution of Combined Heat and Mass Transfer during Film Absorption (in Russian), Izv. Ross. Akad. Nauk, Mekh. Zhidk. Gaza 3 (1977) 893–898.

[6] G. Grossman, Simultaneous Heat and Mass Transfer in Film Absorption Under Laminar Flow, International Journal of Heat and Mass Transfer 26 (1983) 357–371.

[7] N. Brauner, D. Moalem, H. Meyerson, Coupled Heat condensation and mass absorption withcomparable concentrations of absorbate and absorbent., International Journal of Heat and Mass Transfer 32 (1989) 1897–1906.

[8] J. W. Andberg, Absorption of Vapours into Liquid Films Flowing over Cooled Horizontal Tubes, Ph.D. thesis, University of Texas, 1986.

[9] N. Kawae, T. Shigechi, K. Kanemaru, T. Yamada, Water vapor evaporation into laminar film flow of a lithium bromide water solution (influence of variable properties and inlet film thickness on absorption mass transfer rate)., Renewable and Sustainable Energy Reviews 18 (1989) 58–70.

[10] W. A. Miller, H. Pérez-Blanco, V. Patnaik, Advanced Surfaces for Vertical Tube Absorbers. Final Report to the Gas Research Institute, Technical Report, Oak Ridge National Laboratory, 1993.

[11] W. A. Miller, H. Pérez-Blanco, Vertical-Tube Aqueous LiBr Falling Film Absorption Using Advanced Surfaces, in: Proceedings of the International Absorption Heat Pump Conference 1993, pp. 185–202.

[12] H. Takamatsu, H. Yamashiro, N. Takata, H. Honda, Vapor Absorption by LiBr Aqueous Solution in Vertical Smooth Tubes, International Journal of Refrigeration 26 (2003) 659–666.

[13] R. Yang, Heat and Mass Transfer in Laminar Wavy Film Absorption with the Presence of Non-Absorbable Gases, Ph.D. thesis, Arizona State University, 1987.

[14] V. Patnaik, Combined Heat and Mass Transfer in Wavy-Film Absorption, Ph.D. thesis, Pennsylvania State University, 1994.

[15] C. D. Park, T. Nosoko, S. Gima, S. T. Ro, Wave-augmented mass tranfer in a liquid film falling inside a vertical tube, International Journal of Heat and Mass Transfer 47 (2003) 2587–2598.

[16] P. Wayne, Some Theorical and Experimental Observations of the Wave Structure of Falling Film Liquid Films., Industrial and Engineering Chemical Fundamentals 16 (1977) 401–406.

[17] H. Sabir, K. O. Suen, G. A. Vinnicombe, Investigation of effects of wave motion on the performance of a falling film absorber, International Journal of Heat and Mass Transfer 39 (1995) 2463–2477.

[18] W. A. Miller, M. Keyhan, The Effect of Roll Waves on the Hydrodynamics of Falling Films Observed in Vertical Column Absorbers, in: Proceedings of the ASME Advanced Energy Systems Division 2001, pp. 1–12.

[19] R. J. Moffat, Describing uncertainties in experimental results, Exp. Thermal and Fluid Science 1 (1988) 3–17.

[20] H. T. Chua, H. K. Toh, K. C. Malel, Improved thermodynamics property fields of LiBr-$H_2O$ solution., International Journal of Refrigeration 23 (1999) 412–429.

[21] S. M. Deng, W. B. Ma, Experimental studies on the characteristics of an absorber using LiBr/$H_2O$ solution as working fluid., International Journal of Refrigeration 22 (1998) 293–301.

[22] A. Matasuda, K. H. Cjoi, T. Kawamura, Effect of Pressure and Concentration on Performance of a vertical falling-film type of absorber and generator using lithium bromide aqueous solutions., International Journal of Refrigeration 18 (1994) 538–542.

[23] W. A. Miller, The Experimental Analysis of Aqueous Lithium Bromide Vertical Film Absorption, Ph.D. thesis, University of Tennessee, 2000.

[24] M. M. Medrano, Desarollo de un Absorbedor Tubular Vertical Enfriado por Aire para un Climatizador de Absorción de Agua-Bromuro de Litio., Ph.D. thesis, Universitat Rovira i Virgili, 2000.

[25] M. Yuksel, E. Schlunder, Heat and Mass Transfer in Non-isothermal Absorption of Gases in Falling Liquid Films. part i: Experimental Determination of Heat and Mass Transfer Coefficients, Chemical Engineering and Processing: Process Intensification 22 (1987) 193–202.

[26] F. L. Sun Jian, S. Zhang, Experimental study on vertical vapor absorption into libr solution with and without additive, Applied Thermal Engineering 31 (2011) 2850–2854.

[27] I. Greiter, I. Wagner, V. Weiss, A. Gerog, Experimental investigation of heat and mass transfer in horizontal tube falling-film absorber with aqueous solutions, in: International Absorption Heat Pump Conference.

[28] K. Masanori, M. Itsuki, O. Akiharu, F. Kazuhiko, Steam absorption into films of aqueous solution of libr flowing over multiple horizontal pipes, Heat Transfer Japanese Research 25 (1996) 476–485.

[29] S. K. Lee, T. Nagasaki, Water Vapor absorption enhancement in libr/$H_2O$ films falling on horizontal tubes, Experimental Heat Transfer 4 (1991) 331–342.

[30] A. M. I. Mohamed, Experimental study of heat transfer and flow characteristics of liquid falling film on a horizontal fluted tube, Heat Mass Transfer 46 (2010) 841–849.

[31] J. Castro, Simulation of Heat and Mass Transfer Phenomena in the Critical Elements of $H_2O$-LiBr Absorption Cooling Machines. Experimental Validation and Application to Design., Ph.D. thesis, Universitat Politècnica de Catalunya, 2005.

[32] J. Castro, A. Oliva, C. D. Pérez-Segarra, C. Oliet, Modelling of the Heat Exchangers of a Small Capacity, Hot Water Driven, Air-Cooled $H_2O$-LiBr Absorption Cooling Machine, International Journal of Refrigeration 31 (2008) 75–86.

[33] J. U. Brackbill, D. B. Kothe, C. Zemach, Modelling of Wavy Flow in turbulent free falling films., International Journal of Multiphase Flow 15 (1989) 505–520.

[34] R. I. Hirshburg, Laminar Film FLow Phenomena, Theory and Application to the Two-Phase Closed Thermosyphon., Ph.D. thesis, Arizona State University, 1980.

[35] R. I. Hirshburg, L. W. Florschuetz, Laminar Wavy-Film Flow: Part I, Hydrodynamic Analysis., ASME J. Heat Transfer 104 (1982) 452–458.

[36] R. I. Hirshburg, L. W. Florschuetz, Laminar Wavy-Film Flow: Part II, Condensation and Evaporation, ASME J. Heat Transfer 104 (1982) 459–464.

[37] J. Kim, K. Cho, Enhancement of Absorption Performance due to the Film Wave Formation on Vertical Absorber., in: 3rd International Symposium on Two-Phase Flow Modelling and Experimentation., pp. 1–5.

[38] V. Patnaik, H. Pérez-Blanco, A study of absorption enhancement by wavy film flows., International Journal of Heat and Fluid Flow 17 (1995) 63–70.

[39] V. Patnaik, H. Pérez-Blanco, Roll Waves in falling films:an approximate treatment of the velicity field., International Journal of Heat and Fluid Flow 17 (1995) 63–70.

[40] F. W. Pierson, S. Whitaker, Some Theoretical and Experimental Observations of the Wave Structure of Falling Liquid Films., Journal of Fluid Mechanics 16 (1977) 401–407.

[41] V. Y. Shkadov, Wave Flow Regimes of Thin Layer of Viscous Fluid Subject to Gravity, Fluid Dynamics 2 (1967) 43–51.

[42] V. Y. Shkadov, Wave Flow Theory for a Thin Viscous Liquid Layer., Fluid Dynamics 3 (1968) 12–15.

[43] R. Yang, D. Wood, A Numerical Solution of the Wavy Motion on a Falling Liquid Film., Solar Energy 69 (1991) 723–728.

[44] R. Yang, D. Jou, Heat and Mass Transfer on Wavy Film Absorption Process., Solar Energy 71 (1993) 533–538.

[45] S. M. Yih, K. Y. Chen, Gas Absorption Into Wavy and Turbulent Falling Films in a Wetted-Wall Column., Chemical Engineering 17 (1982) 123–136.

[46] B. E. Anshus, On the Asymptotic Solution to the Falling Film Stability Problem., Industrial and Engineering Chemical Fundamentals 11 (1972) 502–508.

[47] C. F. Gerald, Applied Numerical Analysis, Addison-Wesley, 1978.

[48] N. Ablanque, Numerical Simulation and Experimental Validation of Vapor Compression Refrigerating Systems. Special Emphasis on Natural Refrigerants., Ph.D. thesis, Universitat Politècnica de Catalunya, 2010.

[49] O. García-Valladares, Simulación numérica y validación experimental de evaporadores, condensadores y tubos capilares. integración en sistemas de refrigeración por compresión, Ph.D. thesis, Universitat Politècnica de Catalunya, 2000.

[50] S. W. Churchill, Friction-factor equation spans all fluid-flow regimes, Chemical Engineering 84 (1977) 91–92.

[51] V. Gnielinski, New equations for heat and mass transfer in turbulent pipe and channel flow., International Chemical Engineering 16 (1976) 359–368.

[52] S. V. Patankar, Numerical Heat Transfer and Fluid Flow, Hemisphere Publishing Corporation, 1980.

[53] T. Ravigururajan, A. Bergles, Development and Verification of General Correlations for Pressure Drop and Heat Transfer in Singel-Phase Turbulent Flow in Enhanced Tubes, Exp. Thermal and Fluid Science 13 (1996) 55–70.

[54] R. B. Bird, W. E. Stewart, E. N. Lightfoot, Fenómenos de Transporte., REVERTÉ, 1973.

[55] K. E. Herold, R. Radermacher, S. A. Klein, Absorption Chillers and Heat Pumps, CRC Press, 1996.

[56] J. R. Welty, C. E. Wicks, R. E. Wilson, G. L. Rorrer, Fundamentals of momentum, Heat and Mass Transfer, Willey, 2008.

[57] Z. Yuan, K. E. Herold, Thermodynamic properties of aqueous lithium bromide using a multiproperty free energy correlation, HVAC and R Research 11 (2005) 377–393.

[58] R. M. DiGuilio, R. J. Lee, S. M. Jeter, A. S. Teja, Properties of Lithium Bromide-Water Solutions at High Temperatures and Concentrations. I. Thermal Conductivity, ASHRAE Transactions 96 (1990) 702–708.

[59] R. J. Lee, R. M. DiGuilio, S. M. Jeter, A. S. Teja, Properties of Lithium Bromide-Water Solutions at High Temperatures and Concentrations. II. Density and Viscosity, ASHRAE Transactions 96 (1990) 709–714.

[60] Y. Kaita, Thermodynamic Properties of Lithium Bromide-Water Solutions at High Temperatures, International Journal of Refrigeration 24 (2001) 374–390.

[61] L. McNeely, Thermodynamic Properties of Aqueous Solutions of Lithium Bromide, ASHRAE Transactions 85 (1979) 413–434.

[62] M. Wimby, T. Berntsson, Viscosity and density of aqueous solutions of LiBr, LiCl,ZnBrz, $CaCl_2$,and $LiNO_3$, 1, single salt solutions, Journal Chem. Eng 39 (1994) 68–72.

[63] J. Patek, A. Klofar, Acomputationally effective formulation of the thermodynamicproperties of LiBr–$H_2O$ solutions from 273 to 500 k overfull composition range, International Journal of Refrigeration 29 (2006) 566–578.